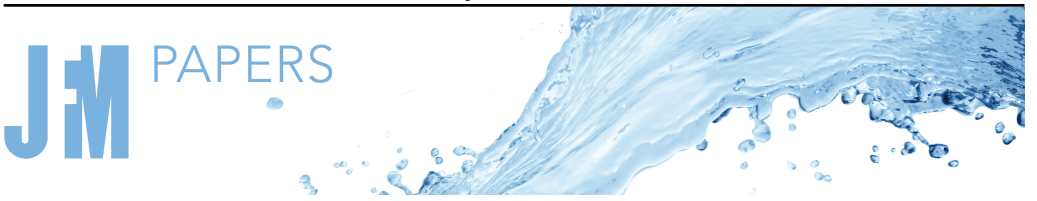
J. Fluid Mech. (2026), *vol.* 1034, A27, doi:10.1017/jfm.2026.11476



Turbulence modulation by Taylor-scale settling particles

Xinyu Jiang[1], **Shahab Mirzareza**[2], **Marco Crialesi Esposito**[3] **and Luca Brandt**[1,2]

[1]Department of Environment, Land and Infrastructure Engineering (DIATI), Politecnico di Torino, Torino 10129, Italy

[2]Department of Energy and Process Engineering, Norwegian University of Science and Technology (NTNU), Trondheim, Norway

[3]Dipartimento di Ingegneria 'Enzo Ferrari', Università di Modena e Reggio Emilia, via Vivarelli 10, Modena 41125, Italy

Corresponding author: Xinyu Jiang, xinyu.jiang@polito.it

(Received 11 September 2025; revised 12 January 2026; accepted 20 March 2026)

In this study, we investigate the modulation of sustained turbulence by settling spherical particles using particle-resolved direct numerical simulations. Gravity effects are studied by varying the Galileo number, *Ga*, through the particle–fluid density ratio for particles of Taylor-scale size. Particle sedimentation causes enhanced viscous dissipation and anisotropy of the fluid velocity fluctuations, which increase with *Ga*. More significantly, the energy spectra exhibit a κ^{-3} scaling, which coexists with the classic $\kappa^{-5/3}$ law for particle-laden turbulence with weak sedimentation ($Ga \lesssim 40$); the κ^{-3} scaling widens its wavenumber range with *Ga* and dominates the energy spectrum at the highest *Ga* under study. The scale-by-scale energy budgets demonstrate that the particle–fluid interactions mainly transfer energy from large to small scales for small settling speeds, whereas the particle sedimentation injects energy into the carrier flow and breaks the isotropic energy distribution for a high *Ga*. In particular, the gravity-induced forcing originates vertically elongated structures while disrupting horizontal flow correlations, thereby altering the nonlinear interscale energy transfer and reshaping the energy spectra. For the solid phase, it is found that the particle vertical velocity fluctuations decrease with *Ga*, and turbulence has a weaker influence on the mean settling velocity for particles with a higher *Ga*. Moderate particle clustering is identified, an observation not changing significantly with the particle settling speed. The collision rate among particles is highest at the strongest particle sedimentation, due to the enhanced relative radial velocity of particle pairs which are preferentially horizontally aligned.

Key words: particle/fluid flows, homogeneous turbulence

© The Author(s), 2026. Published by Cambridge University Press.

https://doi.org/10.1017/jfm.2026.11476 Published online by Cambridge University Press

1. Introduction

The behaviour of suspended particles in turbulent flows is of considerable interest to a variety of processes, including dispersion of aerosols and collisions of water droplets in the atmosphere, sediment transport and ecological processes in the plankton, see e.g. Shaw (2003), Balachandar & Eaton (2010), Guazzelli & Morris (2011) and Ardekani *et al.* (2017). These applications involve complex interactions between the dispersed and carrier phases, which depend on a large number of parameters: the fluid in which the particles are suspended may be quiescent or turbulent; particles may differ in size, shape, density and stiffness; the dispersed particles can sediment under the action of gravity. The range of temporal and spatial scales involved is wide and the global properties of these suspensions can be substantially different from one case to another. Because of these complexities, our general understanding of the problem is still incomplete (Brandt & Coletti 2022).

Solid particles (or droplets) in turbulence are usually categorized by their relative size compared with the smallest turbulent length scale in the dissipative range, the Kolmogorov length scale (Balachandar & Eaton 2010; Dodd & Ferrante 2016). The dynamics of small particles (with the dimension smaller than the Kolmogorov length scale) in homogeneous isotropic turbulence (HIT) has been the object of several earlier studies, see e.g. Squires & Eaton (1990), Elghobashi & Truesdell (1993), Boivin, Simonin & Squires (1998) and Sundaram & Collins (1999). For these particles, the induced turbulence modulation is fully characterized by the ratio of their response time (τ_p) to the Kolmogorov time scale (τ_η), i.e. the Stokes number $St = \tau_p/\tau_\eta$ (Ferrante & Elghobashi 2003; Yang & Shy 2005). It was found that particles with large Stokes numbers tend to suppress the energy of turbulent eddies of all sizes, whereas the opposite is true for particles whose response time is comparable to the Kolmogorov time scale ($St \approx 1$). For particles with intermediate Stokes numbers between these two limits, however, the energy of the large-scale eddies is attenuated, while the energy of the small-scale ones is enhanced (Poelma & Ooms 2006).

When the particle size becomes comparable to or larger than the Kolmogorov length scale (so called finite-size particles), the turbulence modulation cannot be solely predicted by the Stokes number. In this case, changing the particle size or the particle–fluid density ratio has different effects on the turbulence modulation (Lucci, Ferrante & Elghobashi 2011; Chiarini & Rosti 2024). Finite-size particles usually alter the flow structures comparable or smaller than the particle size (Naso & Prosperetti 2010; Homann, Bec & Grauer 2013). For particles of the order of the Kolmogorov length scale, the experiments conducted by Hwang & Eaton (2006) demonstrated the reduced turbulent kinetic energy and dissipation rate when increasing the particle mass loading. Schneiders, Meinke & Schröder (2017) studied decaying turbulence laden with Kolmogorov-scale particles. These authors found that particles absorb energy from the large scales of the carrier phase, whereas the inertial particles increase the local flow dissipation due to the intense strain rate near the particle surfaces. Recently, Chiarini, Tandurella & Rosti (2025) employed the particle-resolved and point-particle approaches to investigate sub-Kolmogorov particles in sustained turbulence. The comparison between these two different numerical approaches demonstrated that the Eulerian and Lagrangian statistics of the particle phase can be well captured with the point-particle simulation for light particles (particle–fluid density ratio $\rho_p/\rho_f = 5$). However, for the heavy particles with $\rho_p/\rho_f \sim 100$, the discrepancy between the two approaches is non-negligible even in dilute cases, since the particle-induced turbulence modulations at small scales in turn alter the particle dynamics.

As regards larger particles with size of the Taylor length scale, plenty of studies have been performed. Using particle-resolved simulations, Ten Cate *et al.* (2004) showed that the presence of particles attenuates the turbulent kinetic energy at large scales

https://doi.org/10.1017/jfm.2026.11476 Published online by Cambridge University Press

and enhances the dissipation rate in the particle boundary layers. Lucci, Ferrante & Elghobashi (2010) numerically investigated the particle-laden decaying turbulence and demonstrated that the increased strain rate in the vicinity of the particle surface enhances the viscous dissipation, an effect becoming more pronounced for particles with higher density. Similarly, Shen *et al.* (2022) and Oka & Goto (2022) also reported the additional energy dissipation in the wake region surrounding the dispersed particles. This mechanism is intensified with increased particle Reynolds number and is responsible for the observed turbulence attenuation (Shen *et al.* 2022). Nevertheless, augmentation of turbulence was also reported due to the vortex shedding of large particles at high particle Reynolds numbers (Gore & Crowe 1989; Hetsroni 1989). More recently, Chiarini & Rosti (2024) numerically studied the turbulence modulation by finite-size particles of different size at a high Taylor Reynolds number $Re_\lambda = 400$. It was found that particles with different sizes and density ratios have different influences on the energy transfer within the carrier fluid: the fluid–solid interactions become important for heavy particles since the viscous dissipation is amplified even in the regions away from highly inertial particles due to the flow separation. To summarize, the occurrence of both turbulence attenuation and augmentation demonstrates the complicated interactions between the particle and fluid phases of different properties. To predict the turbulence modulation, some empirical criteria that combine different governing factors (e.g. particle size, solid–fluid density ratio, particle volume fraction and the flow Reynolds number) have been proposed based on experimental and numerical data (Tanaka & Eaton 2010; Peng, Sun & Wang 2023; Balachandar, Peng & Wang 2024).

From a different perspective, the dynamics and spatial distribution of the finite-size particles are also relevant and significantly influenced by the carrier turbulent flow. Homann & Bec (2010) and Cisse, Homann & Bec (2013) investigated the motion of a single sphere in forced turbulence by means of particle-resolved simulations. These authors found that the particle–fluid slip velocity of neutrally buoyant particles increases with the particle size with a scaling law of $(D/\eta)^{2/3}$. As regards the particle collective behaviour, Fiabane *et al.* (2012) experimentally studied the spatial distribution of finite-sized particles in turbulence, and observed the clustering of particles heavier than the fluid, with the neutrally buoyant particles showing no clustering. Accordingly, it was argued that the Stokes number, which is commonly used to characterize the preferential concentration of heavy small particles in turbulence (Squires & Eaton 1990; Balachandar & Eaton 2010; Monchaux, Bourgoin & Cartellier 2012), is not the most appropriate parameter to predict the spatial distribution of finite-size particles. Note that, particle clustering was also reported in the numerical simulations of finite-size particles in turbulence (Jin *et al.* 2013; Uhlmann & Chouippe 2017; Chiarini & Rosti 2024). The tendency of clustering for particles of Taylor length scale was found to be weakened with increasing particle size (Uhlmann & Chouippe 2017). The collective behaviours of the dispersed particles, in particular the particle clustering and relative motions, play a significant role in the particle collision efficiency, a key issue relevant to a variety of natural and industrial applications (Pumir & Wilkinson 2016).

The problem becomes more complicated when the particle sedimentation is taken into consideration. Without the background turbulent flows, it has been found that settling particles in an initially quiescent fluid can form microstructures with different morphology at varying particle settling Reynolds numbers (Yin & Koch 2007; Uhlmann & Doychev 2014; Zaidi, Tsuji & Tanaka 2014). The drafting–kissing–tumbling (DKT)-related hydrodynamic interactions between settling particles are responsible for the formation of particle microclusters that alter the particle settling rate (Uhlmann & Doychev 2014; Zaidi

https://doi.org/10.1017/jfm.2026.11476 Published online by Cambridge University Press

et al. 2014). The particle shape also plays a significant role once settling is considered, see e.g. Fornari, Ardekani & Brandt (2018), Moriche *et al.* (2023) and Jiang, Zhao & Brandt (2025), yet only spherical particles are considered in this study. Recently, Jiang *et al.* (2025) investigated the pseudoturbulence induced by settling particles. The gravity-driven motion of the particles produces flow fluctuations that are anisotropic along the horizontal and vertical directions, and the particle–fluid interactions are crucial for the energy transfer in the particle-induced pseudoturbulence. When the background turbulence is taken into account, small heavy particles in HIT, typically at volume fraction lower than 10^{-4}, were reported to settle faster than isolated particles in quiescent flows (Wang & Maxey 1993; Aliseda *et al.* 2002; Petersen, Baker & Coletti 2019). This observation was explained by the so-called 'preferential sweeping' effect, i.e. the inertial particles tend to preferentially accumulate in the high-strain regions where downward fluid flows dominate, so the particle settling speed is enhanced (Wang & Maxey 1993). This effect was found to maximize when the particle relaxation time matches the turbulence viscous time, i.e. $St \sim O(1)$. The settling enhancement is further strengthened when the feedback from the particle to the carrying flow is non-negligible, since the settling particles drag the surrounding fluid downwards, which in turn accelerates the particle settling motions (Bosse, Kleiser & Meiburg 2006; Monchaux & Dejoan 2017; Huck *et al.* 2018; Tom, Carbone & Bragg 2022; Bhattacharjee *et al.* 2024). However, opposite is true for finite-size particles. By virtue of the particle-resolved simulations, the mean settling velocity of particles of $D \sim O(10)\eta$ in HIT was found to be lower than that of the isolated particle settling in the quiescent fluid (Chouippe & Uhlmann 2015; Fornari *et al.* 2016*a*,*b*, 2019). The nonlinear and unsteady effects increase the drag acting on settling particles in turbulent flows, so as to reduce the particle settling velocity (Chouippe & Uhlmann 2015; Fornari *et al.* 2016*b*; Peng *et al.* 2025). Furthermore, the collision rate of the settling particles was found to be reduced in dilute cases, mainly due to the less frequent DKT in the presence of turbulence; conversely, the turbulent transport enhances the relative motion between particles in dense suspensions, leading to an increase in the collision rate compared with that in the quiescent fluid (Fornari *et al.* 2019).

Despite the studies reviewed above, the turbulence modulation by finite-size settling particles has not been thoroughly investigated so far. From dimensional analysis, homogeneous turbulence laden with settling finite-size particles is governed by five dimensionless parameters, namely the Taylor-scale Reynolds number Re_λ, the particle-to-Kolmogorov size ratio D/η, the particle-to-fluid density ratio ρ_p/ρ_f, the particle volume fraction ϕ and the Galileo number Ga, instead of simply the Stokes number and volume and mass loadings as in the point-particle-laden turbulence (Brandt & Coletti 2022). The Galileo number Ga here is a dimensionless parameter measuring the buoyancy and viscous force acting on settling particles, see § 2 for the concrete definition. Especially, how the turbulence intensity and the energy transfer in the carrier flow change with the particle settling velocity, which is relevant in many practical applications, yet remains unclear. Therefore, in this study, we aim to explore the effect of sedimentation velocity on the particle-induced turbulence modulation. To this end, we perform particle-resolved direct numerical simulations (PR-DNS) of finite-size particles settling in sustained HIT over a range of Galileo numbers $Ga \in [0, 120]$. Variations in Ga are achieved by changing the particle–fluid density ratio while keeping the particle diameter fixed at the Taylor microscale (i.e. $O(10)$ Kolmogorov length scales). In contrast to previous PR-DNS studies of settling particles in HIT, which mostly considered dilute suspensions with $\phi < 0.5\,\%$ (Chouippe & Uhlmann 2015; Fornari *et al.* 2016*b*; Peng *et al.* 2025), we focus on a non-dilute regime at $\phi = 10\,\%$. This choice of volume fraction allows for an appreciable modulation of the background turbulence by the settling particles. In particular, we observe

https://doi.org/10.1017/jfm.2026.11476 Published online by Cambridge University Press

a pronounced reshaping of the energy spectrum, including the emergence of a κ^{-3} scaling and marked anisotropy of energy distribution at intermediate scales. A scale-by-scale (SBS) energy budget analysis is conducted to study the underlying mechanisms. Apart from the fluid phase, the particle-phase statistics, including the settling velocity reduction, clustering and collision rate, are also investigated and compared with previous studies.

The remainder of this paper is organized as follows. In § 2, we briefly introduce the numerical method and the analysis tools employed in this study. Then, in § 3, we present the results of the simulations, including the statistics of the fluid flow and particle motion, the energy spectra and energy transfer within the carrier flows, and document the particle clustering and collision rates. Finally, we draw the main conclusion of this work in § 4.

2. Methodology

2.1. *Governing equations and numerical methods*

In the present study, we use the PR-DNS based on the immersed boundary method (IBM) to simulate the turbulent flow laden with finite-size particles. The fluid flow is governed by the incompressible Navier–Stokes (NS) equations as follows:

$$\nabla \cdot \boldsymbol{u} = 0, \tag{2.1}$$

$$\frac{\partial \boldsymbol{u}}{\partial t} + \boldsymbol{u} \cdot \nabla \boldsymbol{u} = -\frac{1}{\rho_f}\nabla p + \nu \nabla^2 \boldsymbol{u} + \boldsymbol{f}_{ext} + \boldsymbol{f}_{ib} - \langle \boldsymbol{f}_{ib} \rangle_{\Omega}. \tag{2.2}$$

Here, $\boldsymbol{u} = [u_x, u_y, u_z]$ is the fluid velocity vector, p is the pressure, and ρ_f and ν denote the density and kinematic viscosity of the Newtonian fluid. In (2.2), the body forcing term $\boldsymbol{f}_{ext}$ represents the external forces that sustain the turbulent flow. Specifically, we employ the method proposed initially by Eswaran & Pope (1988) to compute $\boldsymbol{f}_{ext}$ (denoted as 'EP' forces hereinafter). In brief, the body forces are obtained in the physical space from the inverse Fourier transformation of a set of random forces $\hat{\boldsymbol{f}}$ defined on $\|\boldsymbol{\kappa}\| \leqslant \kappa_f$ in the spectral space. Here, κ_f is the cutoff wavenumber; the random forces are generated in the spectral space with Ornstein–Uhlenbeck processes. The readers are referred to Eswaran & Pope (1988) and Chouippe & Uhlmann (2015) for more details about the computation of $\boldsymbol{f}_{ext}$.

The other forcing term $\boldsymbol{f}_{ib}$ in (2.2) denotes the immersed-boundary (IB) forcing term for modelling the particle–fluid interactions. In particular, we employ the direct-forcing IBM with multiforcing corrections (Uhlmann 2005; Breugem 2012). Note that the spatial average of the IB forcing term, $\langle \boldsymbol{f}_{ib} \rangle_{\Omega}$, is subtracted from the momentum (2.2) to retain the zero net flow rate (i.e. $\langle \boldsymbol{u} \rangle_{\Omega} = 0$) for simulations conducted in a triperiodic computational domain (Höfler & Schwarzer 2000; Chouippe & Uhlmann 2015).

As concerns the numerical algorithm, we employ a projection-based finite difference method to numerically solve the incompressible NS equations (2.1)–(2.2), see the original work by Kim, Baek & Sung (2002). Specifically, the second-order central difference is employed for the spatial discretization, while the Crank–Nicolson temporal discretization is used for the diffusion and advection terms, leading to a fully implicit advancement in time. After obtaining the predicted velocity by integrating the diffusion and nonlinear terms, a Poisson equation is solved with the fast Fourier transformation algorithm to impose the divergence-free constraint. These schemes retain the second-order accuracy in both time and space (Kim *et al.* 2002). For more details and validations of the present numerical method, the readers are referred to our previous publications (Jiang, Xu & Zhao 2024*a*,*b*).

https://doi.org/10.1017/jfm.2026.11476 Published online by Cambridge University Press

Case	ρ_p/ρ_f	Ga	Re_{s0}	V_{s0}/u_0'	$L_x \times L_y \times L_z$	$N_x \times N_y \times N_z$	$\eta/\Delta x$	$\kappa_{max}\eta$	N_p
0	—	—	—	—	$32D \times 32D \times 32D$	$256 \times 256 \times 256$	0.59	1.85	0
1	1.0	0	0	0	$32D \times 32D \times 32D$	$512 \times 512 \times 512$	1.23	3.86	6258
2	1.020	40	32.5	0.46	$32D \times 64D \times 32D$	$512 \times 1024 \times 512$	1.22	3.83	12516
3	1.082	80	85.0	1.20	$32D \times 64D \times 32D$	$512 \times 1024 \times 512$	1.07	3.36	12516
4	1.183	120	146.0	2.05	$32D \times 64D \times 32D$	$768 \times 1536 \times 768$	1.30	4.08	12516

Table 1. Simulation set-ups. Here, ρ_p/ρ_f denotes the density ratio between the particle and fluid; Ga is the Galileo number; Re_{s0} is the Reynolds number defined by the settling velocity V_{s0} of an isolated particle; L_i (with $i = x$, y or z) is the length of the computational domain; N_i is the number of grid cells along the i-direction; N_p is the number of particles in the simulation.

The translational and rotational motions of the dispersed particles are governed by the classic Newton–Euler equations:

$$\rho_p V_p \frac{\mathrm{d}\boldsymbol{v}}{\mathrm{d}t} = \boldsymbol{F}_H + \left(\rho_p - \rho_f\right)\boldsymbol{g} V_p + \boldsymbol{F}_C, \tag{2.3}$$

$$I_p \frac{\mathrm{d}\boldsymbol{\omega}}{\mathrm{d}t} = \boldsymbol{T}_H + \boldsymbol{T}_C. \tag{2.4}$$

Here, $\boldsymbol{v} = [v_x, v_y, v_z]$ and $\boldsymbol{\omega} = [\omega_x, \omega_y, \omega_z]$ denote the particle linear and angular velocity, respectively. The symbols ρ_p, V_p and I_p represent the density, volume and moment of inertia of the particle, namely $V_p = \pi D^3/6$ and $I_p = \rho_p V_p D^2/10$ for a sphere; $\boldsymbol{g}$ is the gravity acceleration. The hydrodynamic force and torque acting on the dispersed particles, denoted by $\boldsymbol{F}_H$ and $\boldsymbol{T}_H$, are obtained by integrating the IB forces (Breugem 2012; Kempe & Fröhlich 2012). The contact force and torque $\boldsymbol{F}_C$ and $\boldsymbol{T}_C$, which account for the particle–particle collisions, are modelled by the soft-sphere collision forces with lubrication correction (Jeffrey 1982; Costa *et al.* 2015).

2.2. *Simulation set-ups*

The simulation cases and set-ups of the present study are summarized in table 1. Before examining the particle-laden flows, we first run one simulation of the single-phase turbulent flow, denoted by 'case 0' in table 1, as a reference case. The parameters related to the EP forces are listed in table 2, including the cutoff wavenumber κ_f, the time scale of the Ornstein–Uhlenbeck process T_L and the amplitude of the random forces σ (see more details concerning the definition of these variables in Eswaran & Pope (1988) and Chouippe & Uhlmann (2015)). The statistics of the single-phase turbulence obtained with these EP parameters, including the root-mean-square (r.m.s.) velocity fluctuation u', the mean dissipation rate ϵ, the Kolmogorov length scale $\eta = \nu^{3/4}\epsilon^{-1/4}$, the Taylor micro scale $\lambda = \sqrt{15\nu u'^2\epsilon^{-1}}$, the integral length scale $L_{int} = (3u'^2/2)^{3/2}\epsilon^{-1}$, the Kolmogorov time scale $\tau_\eta = \nu^{1/2}\epsilon^{-1/2}$, the turn-over time scale $T_e = u'^2/\epsilon$ and the Taylor Reynolds number $Re_\lambda = u'\lambda/\nu$, are also provided in table 2. Note that the parameters related to the EP forces are kept constant in the particle-laden cases introduced below.

Given the complexity of the current problem (with five governing parameters as stated in the introduction), the objective of the present study is to shed some light on the effect of the sedimentation velocity on the particle dynamics and turbulence modulation in HIT, while the other properties (i.e. the background turbulence intensity, particle size and particle volume fraction) are kept constant. To this end, we design four simulation cases of particle-laden turbulence with varying Galileo numbers, which is realized by adjusting the particle–fluid density ratio ρ_p/ρ_f, as shown in table 1. The dimensionless

https://doi.org/10.1017/jfm.2026.11476 Published online by Cambridge University Press

κ_f/κ_{x0}	$T_L\nu/L_x^2$	$\epsilon^* L_x^4/\nu^3$	$Re_{\lambda 0}$	$u_0'\tau_p/D$	$\epsilon_0\tau_p^3/D^2$	η_0/D	λ_0/D	$L_{int,0}/D$	$\tau_{\eta,0}/\tau_p$	$T_{e,0}/\tau_p$
2.5	3.02×10^{-4}	8.05×10^{8}	103.4	0.783	5.652	0.074	1.485	18.82	0.099	2.648

Table 2. Parameters used to generate the external forces that sustain the turbulent flow and the statistics of the single-phase turbulence (denoted by the subscript '0'). Here, $\kappa_{x,min} = 2\pi/L_x$ is the fundamental wavenumber along the x-direction, $\epsilon^* = \sigma^2 T_L$ is a bundled parameter (see Chouippe & Uhlmann 2015) and the time scale $\tau_p = D^2/18\nu$ represents the relaxation time of the neutrally buoyant particles.

parameter Ga, defined by $Ga = \sqrt{(\rho_p/\rho_f - 1)gD^3}/\nu$, measures the ratio between the buoyant and viscous force acting on a settling particle in a viscous fluid. The values of Ga are selected by considering spherical particles with a fixed diameter $D = 2$ mm settling in a Newtonian fluid with kinematic viscosity $\nu = 1\times10^{-6}$ m^2 s^{-1}, and gravity acceleration $\|\boldsymbol{g}\| = 9.81$ m s^{-2}. The particle size is of the order of the Taylor microscale of the single-phase turbulence with $D \approx 0.67\lambda_0 \approx 13.5\eta_0$ (see table 1), and the particle volume fraction is fixed at $\phi = N_p V_p/V_\Omega = 10\,\%$ (where $V_\Omega = L_x L_y L_z$ is the total volume of the domain). Note that the change of the particle–fluid density ratio is relatively small, with values $\rho_p/\rho_f \in [1, 1.18]$, indicating a minimal effect of the particle inertia on the results. The choice of parameters mimics slightly buoyant particles in liquid turbulent environments, which is relevant to realistic applications like the microplastic in the ocean, sediment transport and marine snow. The Taylor Reynolds number is chosen to be computationally affordably high while the particle volume fraction is set sufficiently high to induce appreciable turbulence modulation.

The particle settling Reynolds number $Re_{s0} = V_{s0}D/\nu$, which is defined by the settling velocity of an isolated particle without turbulence, V_{s0}, is solely determined by the Galileo number. Here, we estimate the values of Re_{s0} at different Ga by using the following empirical correlation (Yin & Koch 2007):

$$Ga^2 = 18Re_{s0}\left[1 + 0.1935Re_{s0}^{0.6305}\right], \quad \text{for} \quad 20 < Re_{s0} < 260. \tag{2.5}$$

As shown also in table 1, the settling Reynolds number increases with the Galileo number, which also results in an increase of the ratio between the settling velocity and the r.m.s. velocity of the background turbulent flow, V_{s0}/u_0'. This is a fundamental parameter that we will use to analyse the turbulence modulation by settling particles.

The grid resolutions are set as $D = 16\Delta x$ in cases 1–3 and $D = 24\Delta x$ in case 4 due to the higher settling Reynolds number. In table 1, we also list the ratio between the Kolmogorov length scale and the grid width for each case to demonstrate the sufficient resolution for solving the background turbulent flow, following the criterion of $\kappa_{max}\eta = \pi\eta/\Delta x \geqslant 1.5$ (Pope 2000). The simulations are conducted in a triperiodic computational domain with the gravity applied along the negative y-direction. To minimize the impact of domain periodicity for the cases with particle sedimentation, we elongate the domain along the vertical direction (i.e. $L_y = 2L_x$) in cases 2–4, following the suggestions in Chouippe & Uhlmann (2015).

2.3. *Data analysis: SBS spectral analysis*

In § 3.3 we will examine the turbulence modulation by means of the SBS analysis in the spectral space. Here we briefly introduce this approach. By multiplying the Fourier transformation of the momentum (2.2) with the complex conjugate of the velocity vector, we obtain the following energy equation for the fluid flow (Frisch 1995; Crialesi-Esposito

https://doi.org/10.1017/jfm.2026.11476 Published online by Cambridge University Press

et al. 2022):

$$\frac{\partial E(\boldsymbol{\kappa}, t)}{\partial t} = \mathcal{F}_{ext}(\boldsymbol{\kappa}, t) + \mathcal{F}_{ib}(\boldsymbol{\kappa}, t) + \Pi(\boldsymbol{\kappa}, t) + \mathcal{D}(\boldsymbol{\kappa}, t). \tag{2.6}$$

The definition and physical interpretation of the terms $E(\boldsymbol{\kappa}, t)$, $\mathcal{F}_{ext}(\boldsymbol{\kappa}, t)$, $\mathcal{F}_{ib}(\boldsymbol{\kappa}, t)$, $\Pi(\boldsymbol{\kappa}, t)$ and $\mathcal{D}(\boldsymbol{\kappa}, t)$ are as follows:

(i) $E(\boldsymbol{\kappa}, t) = (1/2)\widetilde{\boldsymbol{u}} \cdot \widetilde{\boldsymbol{u}}^*$ is the energy spectrum;
(ii) $\Pi(\boldsymbol{\kappa}, t) = -(1/2)(\widetilde{\boldsymbol{u}}^* \cdot \widetilde{\boldsymbol{G}} + \widetilde{\boldsymbol{u}} \cdot \widetilde{\boldsymbol{G}}^*)$ is the spectrum of the energy transfer by the advective transport, with $\boldsymbol{G} = \boldsymbol{u} \cdot \boldsymbol{\nabla} \boldsymbol{u}$ denoting the nonlinear term of the NS equations;
(iii) $\mathcal{D}(\boldsymbol{\kappa}, t) = (1/2)(\widetilde{\boldsymbol{u}}^* \cdot \widetilde{\boldsymbol{V}} + \widetilde{\boldsymbol{u}} \cdot \widetilde{\boldsymbol{V}}^*)$ is the spectrum of the viscous dissipation, with $\boldsymbol{V} = (1/\nu)\nabla^2 \boldsymbol{u}$ denoting the viscous term;
(iv) $\mathcal{F}_{ib}(\boldsymbol{\kappa}, t) = (1/2)(\widetilde{\boldsymbol{f}_{ib}} \cdot \widetilde{\boldsymbol{u}}^* + \widetilde{\boldsymbol{f}_{ib}}^* \cdot \widetilde{\boldsymbol{u}})$ is the spectrum of the work of the IB forcing term, which reflects the particle–fluid interactions;
(v) $\mathcal{F}_{ext}(\boldsymbol{\kappa}, t) = (1/2)(\widetilde{\boldsymbol{f}_{ext}} \cdot \widetilde{\boldsymbol{u}}^* + \widetilde{\boldsymbol{f}_{ext}}^* \cdot \widetilde{\boldsymbol{u}})$ is the spectrum of the energy production by the external EP forces.

Here, the notation $\tilde{g} = \tilde{g}(\boldsymbol{\kappa}, t)$ indicates the Fourier mode of an arbitrary physical-space variable $g(\boldsymbol{x}, t)$, and the superscript '$*$' denotes the complex conjugate. In practice, the wavenumber vector $\boldsymbol{\kappa} = (\kappa_x, \kappa_y, \kappa_z)$ is defined on discrete grid points in the spectral space, i.e. $\boldsymbol{\kappa}_{lmn} = (\kappa_{x,l}, \kappa_{y,m}, \kappa_{z,n}) = (l\Delta\kappa_x, m\Delta\kappa_y, n\Delta\kappa_z)$ (with the indices $l = -N_x/2 + 1, \cdots, N_x/2$, $m = -N_y/2 + 1, \cdots, N_y/2$, $n = -N_z/2 + 1, \cdots, N_z/2$ and the wavenumber increment $\Delta\kappa_i = 2\pi/L_i$). Note that the pressure term (the first term on the right-hand side of (2.2)) vanishes in the energy budget of an incompressible flow (Pope 2000), and the subtracted spatially averaged IB forcing term $\langle \boldsymbol{f}_{IB} \rangle_\Omega$ also has a zero contribution to the energy budget. Moreover, after the flow system reaches the steady state, the different terms on the right-hand side of (2.6) balance each other, with $\partial E(\boldsymbol{\kappa}, t)/\partial t = 0$. In what follows, we shall omit the independent variable t and express the spectra only as function of the wavenumber; the statistics are computed by the time average at the steady state.

To understand the energy budget on the different scales, the most common approach is to compute the energy as function of the wavenumber magnitude $|\boldsymbol{\kappa}|$ by performing an integral over a spherical-shell of radius $|\boldsymbol{\kappa}|$ for any arbitrary variable $\mathcal{J}(\boldsymbol{\kappa})$ ($\mathcal{J}(\boldsymbol{\kappa})$ can stand for $E(\boldsymbol{\kappa})$, $\mathcal{F}_{ext}(\boldsymbol{\kappa})$, $\mathcal{F}_{ib}(\boldsymbol{\kappa})$ or $\mathcal{D}(\boldsymbol{\kappa})$ or $\Pi(\boldsymbol{\kappa})$), i.e. (Pandey, Ramadugu & Perlekar 2020)

$$\mathcal{J}(\kappa) = \sum_{\kappa - 0.5\Delta\kappa \leqslant \|\boldsymbol{\kappa}'\| < \kappa - 0.5\Delta\kappa} \mathcal{J}(\boldsymbol{\kappa}'), \tag{2.7}$$

where $\Delta\kappa = \max\{\Delta\kappa_x, \Delta\kappa_y, \Delta\kappa_z\}$. However, with the introduction of gravity, the isotropy of the spectra in the spectral space would be broken. Hence, to additionally provide the directional information of an anisotropic spectrum, we adopt as independent variables the horizontal and vertical wavenumbers and define a two-dimensional function of the spectral density (with notation $\tilde{\cdot}$) as

$$\tilde{\mathcal{J}}(\kappa_h, \kappa_y) = \frac{1}{N_h(\kappa_h, \kappa_y)} \sum_{\kappa_h - 0.5\Delta\kappa_h \leqslant \sqrt{\kappa_x^2 + \kappa_z^2} < \kappa_h + 0.5\Delta\kappa_h} \tilde{\mathcal{J}}(\kappa_x, \kappa_y, \kappa_z). \tag{2.8}$$

Here, we compute the average of the spectral density $\tilde{\mathcal{J}}(\boldsymbol{\kappa}) = \mathcal{J}(\boldsymbol{\kappa})/(\Delta\kappa_x \Delta\kappa_y \Delta\kappa_z)$ only over the (isotropic) horizontal directions (i.e. on the planes perpendicular to the gravity

https://doi.org/10.1017/jfm.2026.11476 Published online by Cambridge University Press

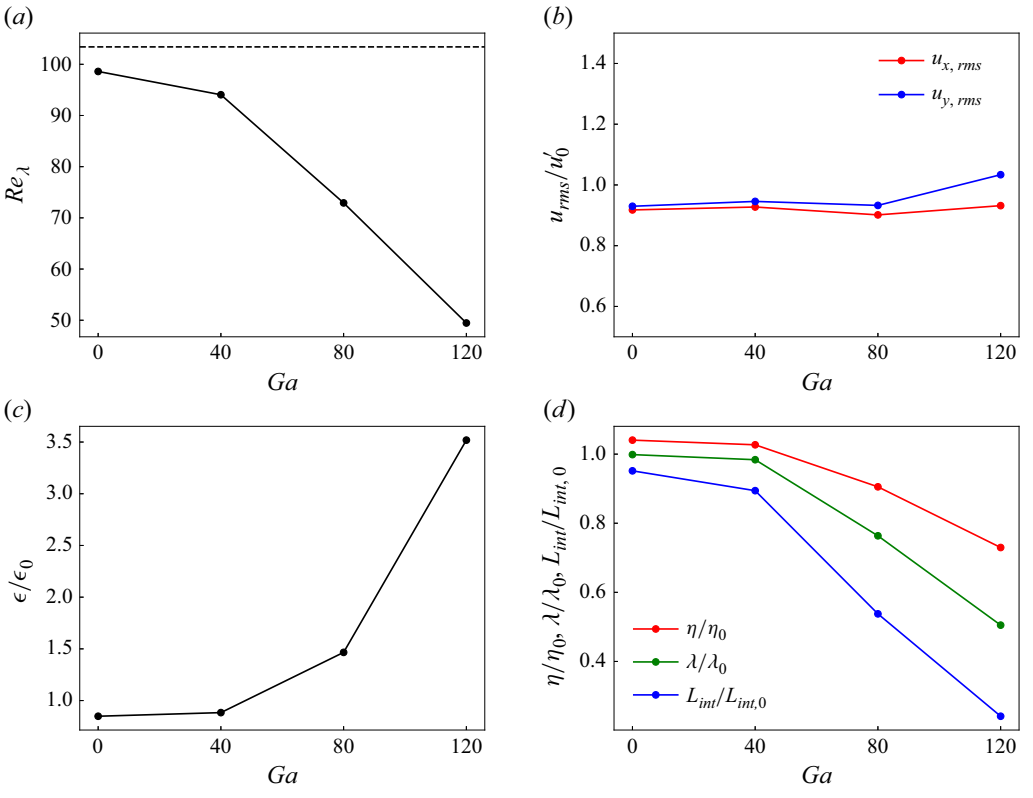


Figure 1. (*a*) Taylor Reynolds number Re_λ versus Galileo number. The black dashed line represents the data of the single-phase turbulence. (*b–d*) The change of the (*b*) r.m.s. velocity fluctuations, (*c*) mean dissipation rate and (*d*) length scales of the turbulent flow as Ga increases. In panels (*b*)–(*d*) the results are normalized by the value of the single-phase turbulence.

direction). In the definition (2.8), κ_h represents the horizontal wavenumber with $\Delta\kappa_h = \Delta\kappa_x = \Delta\kappa_z$, and $N_h(\kappa_h, \kappa_y)$ denotes the number of modes satisfying $\kappa_h - 0.5\Delta\kappa_h \leqslant \sqrt{\kappa_x^2 + \kappa_z^2} < \kappa_h + 0.5\Delta\kappa_h$ for any given κ_y.

3. Results

3.1. *Statistics of the fluid flow*

We first report the global statistics of the turbulent flows modulated by the dispersed particles, with the results presented in figure 1. First, we can observe from figure 1(*a*) that the Taylor Reynolds number is smaller for the particle-laden flows than for the single-phase turbulence, and the value of Re_λ decreases with Ga. To interpret the change of the Taylor Reynolds number, we compute the velocity fluctuations and the mean dissipation rate of the fluid flow. As shown in figure 1(*b*), the modulation of the fluid velocity fluctuations by the presence of particles is rather small. The presence of non-settling particles ($Ga = 0$) slightly reduces the r.m.s. of the turbulent flow, indicating the turbulence attenuation. In the cases with non-zero Galileo numbers, the introduction of gravity increases the vertical velocity fluctuation for higher Ga, while the horizontal velocity fluctuation does not change significantly. Consequently, the turbulent flow becomes anisotropic in the suspension of settling particles, an observation that was also reported in the case of

https://doi.org/10.1017/jfm.2026.11476 Published online by Cambridge University Press

Case	Ga	$(k_{PL}/k_{SP})_{DNS}$	$(k_{PL}/k_{SP})_{model}$
1	0	0.876	0.942
2	40	0.898	0.922
3	80	0.857	1.188
4	120	0.963	1.455

Table 3. Turbulence modulation by the dispersed particles. The results of the present simulations are denoted by the subscript 'DNS' and compared with the theoretical model by Balachandar *et al.* (2024), indicated by the subscript '$model$'.

a turbulent flow modulated by small settling particles (Bhattacharjee *et al.* 2024). The greater vertical velocity fluctuation can be ascribed to the conversion of the gravity potential energy to turbulence kinetic energy by the particle settling motions. Without the background turbulence, the fluid flow solely induced by the gravity-driven motion of light bubbles or heavy particles (the so-called pseudoturbulence) is also reported to be anisotropic with larger velocity fluctuations along the direction of gravity (Fornari *et al.* 2016*a*; Amoura *et al.* 2017; Jiang *et al.* 2025). However, the degree of anisotropy is rather low in the present configuration, with the value of $u_{y,rms}/u_{x,rms}$ being only 1.09 in the case with the largest settling speed, $Ga = 120$, while it was found to be larger than 2.5 for the particle-induced pseudoturbulence in quiescent fluids (Jiang *et al.* 2025). This is presumably due to the enhanced energy redistribution among the different velocity components by the background turbulent flow.

The particle-induced turbulence modulation is quantified by the ratio of the turbulent kinetic energy of the particle-laden flow and the single-phase flow, denoted by k_{PL}/k_{SP}. Turbulence attenuation is identified when the ratio is less than unity, while $k_{PL}/k_{SP} > 1$ indicates turbulence augmentation (Yu *et al.* 2021). The values of this ratio are presented in table 3 for different cases under study, where we also compare the present simulation results with the theoretical model in Balachandar *et al.* (2024). This model predicts the turbulence modulation by the particle phase based on six input parameters: (i) the ratio between the particle size and the Kolmogorov length scale; (ii) the Taylor Reynolds number; (iii) the particle volume fraction; (iv) the mean slip velocity between the particle and fluid phases; (v) the particle-to-fluid density ratio; (vi) the ratio of the viscous dissipation of the particle-laden and single-phase turbulence (see more details in Balachandar *et al.* (2024)). As we can see from table 3, this model suggests turbulence attenuation for the cases without or with weak particle sedimentation (cases 1 and 2 with $Ga = 0$ and 40), which are in good agreement with the simulation results. However, the model mistakenly predicts turbulence augmentation at $Ga = 80$ and 120, when the ratio k_{PL}/k_{SP} remains lower than unity according to the simulation data. This disagreement suggests the need of some model improvement for high-Ga scenarios where significant particle–fluid slip is caused by the relatively fast sedimentation. Note that the model in Balachandar *et al.* (2024) was mainly verified against experimental/simulation data without particle settling.

In contrast to the velocity fluctuations, the mean dissipation rate of the fluid flow increases significantly as Ga grows, see figure 1(*c*); this increase is more than linear with Ga and is related to the increase of the system energy supply due to the gravitational settling. A similar enhancement of the dissipation rate was also reported in HIT laden with sub-Kolmogorov settling particles. This effect becomes more prominent for highly inertial particles at a relatively high concentration (see Bhattacharjee *et al.* 2024), but the degree of dissipation enhancement is generally lower in Bhattacharjee *et al.* (2024),

https://doi.org/10.1017/jfm.2026.11476 Published online by Cambridge University Press

probably because of the lower volume fraction in the point-particle simulations. Since the Taylor Reynolds number is related to the dissipation rate by $Re_\lambda \propto \epsilon^{-1/2}$, the enhancement of the dissipation rate gives rise to the reduction of Re_λ with increasing Ga. In the cases with particle sedimentation ($Ga > 0$), the slip velocity between the particle and the local fluid flow results in shear layers in the vicinity of the particle interface, and thus produces the additional viscous dissipation in this region (Lucci *et al.* 2010; Fornari *et al.* 2016*a*; Chiarini & Rosti 2024). As the particle settling velocity further increases, the fluid dissipation rate can be considerably enhanced near the separation region of the particle wakes when the particle Reynolds number is greater than $O(100)$ (Chiarini & Rosti 2024). Therefore, the mean dissipation rate increases rapidly at $Ga \geqslant 80$, which finally balances with the additional energy input from the particles' gravitational energy. Note also that we observe a slight reduction of the viscous dissipation rate compared with the single-phase turbulence in the cases with $Ga = 0$ and $Ga = 40$. The particle–fluid slip velocity is rather small in these cases, so the aforementioned mechanism of the wake-related viscous dissipation is negligible. As a matter of fact, in these two cases, the additional particle-induced dissipation (as elaborated in the following section) partially balances the energy input, so as to reduce the fluid viscous dissipation rate.

The enhanced dissipation rate also results in the reduction in the length scales of the turbulence as classically defined for single-phase flows (figure 1*d*). As confirmed later by the energy spectra (shown and discussed in § 3.3.1), smaller scales are dynamically active in the presence of particles. We recall here that the Taylor Reynolds number is commonly interpreted as the ratio between the largest and smallest scale in single-phase HIT. From the current data, we observe that, given the same large-scale forcing, the dissipative scale decreases in the presence of particles (see also the energy spectra and spectrum of the viscous dissipation below), which would suggest an increase of Re_λ. This is, however, not the case, which indicates that different definitions of these global measures may be required for multiphase flows.

To confirm this first picture of the flow, we provide a visualization of the instantaneous vorticity structures of the fluid flows in cases 0, 1 and 4 in figure 2. Compared with the single-phase turbulence shown in figure 2(*a*), the presence of non-settling particles ($Ga = 0$ case displayed in figure 2*b*) slightly reduces the size of the turbulence coherent structures, a difference not obvious in the figure. However, it is easier to observe more fragmented flow structures in the case with non-negligible particle sedimentation ($Ga = 120$, in figure 2*c*,*d*).

3.2. *Statistics of particle motions*

Next, we examine the statistics of the particle motion. The first observation concerns the particle settling velocity in the turbulent flow. In figure 3(*a*) we present the time history of the particle-averaged (denoted by $\langle\cdot\rangle_p$) velocity of the dispersed particles along the vertical direction, normalized by the settling velocity of an isolated particle in a quiescent fluid, V_{s0}. As expected, $\langle V_s\rangle_p$ fluctuates around zero at $Ga = 0$, since the particle motion is driven by a turbulent flow with zero mean flow. In contrast, for the cases with non-zero Galileo numbers, the settling velocity of the dispersed particles increases from zero to a steady-state value within an interval of approximately $2T_{e,0}$. After that, $\langle V_s\rangle_p$ fluctuates around a constant value so that we can define its time-averaged value as the particle mean settling velocity in suspension, denoted by $\langle V_s\rangle$. The values of $\langle V_s\rangle$ are displayed by closed squares in figure 3(*b*) for the cases under investigation: it is noteworthy that the mean settling velocity in suspensions is smaller than the settling velocity of the isolated particle, regardless of the Galileo number. However, the ratio between $\langle V_s\rangle$ and V_{s0} is an increasing function of the Galileo number.

https://doi.org/10.1017/jfm.2026.11476 Published online by Cambridge University Press

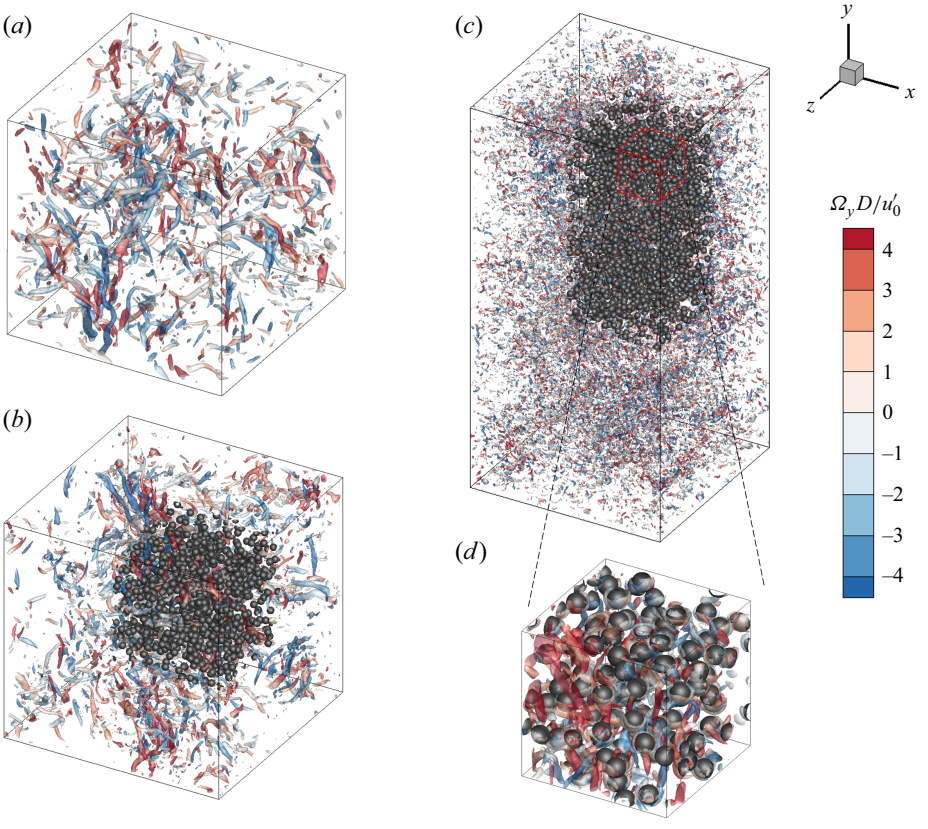


Figure 2. Snapshot of the three-dimensional flow field for (*a*) the single-phase turbulence, (*b*) the particle-laden flow with $Ga = 0$ and (*c*,*d*) the case with particle sedimentation at $Ga = 120$. The isosurfaces of the Q criterion (with $Q = 5u_0'^2/D^2$ in panels (*a*), (*b*) and (*d*), and $Q = 20u_0'^2/D^2$ in panel (*c*)) coloured with the y-vorticity Ω_y are used to visualize the vorticity structures in the flow. The dispersed particles (only within the region $[L_x/2, L_x] \times [L_y/2, L_y] \times [L_z/2, L_z]$ in panels (*b*) and (c) are visualized with the black colour. Panel (*d*) is the zoom-in view of (*c*) within the box (highlighted by the red cube) of size $8D \times 8D \times 8D$.

Let us elaborate on the reduction of the particle settling speed in the current flow configuration. Firstly, we recall that the hindrance effect, which has been extensively studied for the particle sedimentation in a quiescent fluid, is responsible for the decreased settling velocity in suspensions (Richardson & Zaki 1954; Davis & Acrivos 1985; Yin & Koch 2007). It was proposed by Richardson & Zaki (1954) that the hindered settling velocity, the average settling velocity in a suspension, decreases with the particle volume fraction, following the empirical correlation

$$\langle V_s \rangle_{hindered} / V_{s0} = (1 - \phi)^n, \tag{3.1}$$

where the exponent n can be expressed as a function of the settling Reynolds number Re_{s0} (defined based on the isolated-particle settling velocity V_{s0}) (Garside & Al-Dibouni 1977):

$$\frac{5.1 - n}{n - 2.7} = 0.1 Re_{s0}^{0.9}. \tag{3.2}$$

We therefore also depict the hindered settling velocities estimated by (3.1) in figure 3(*b*) with open circles. Interestingly, $\langle V_s \rangle_{hindered}$ still overestimates the mean settling velocity of the present simulations. There must therefore be a second mechanism active to reduce

https://doi.org/10.1017/jfm.2026.11476 Published online by Cambridge University Press

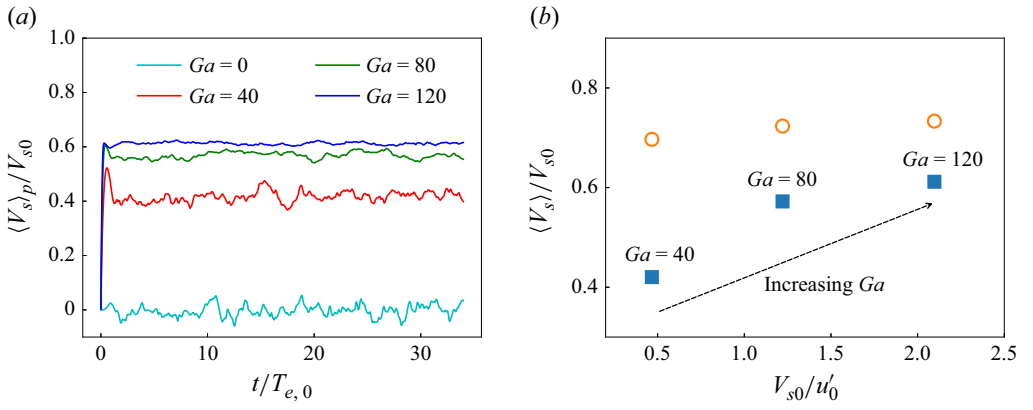


Figure 3. (*a*) Time history of the particle-averaged settling velocity. Here, $\langle V_s\rangle_p$ is normalized by the respective isolated settling velocity V_{s0} for each case (except for the $Ga = 0$ case in which the isolated settling velocity of $Ga = 40$ is used for normalization since $V_{s0} = 0$ for zero Galileo number), while time is normalized by the turn-over time scale of the single-phase turbulence, $T_{e,0}$. (*b*) Closed squares, the ratio between the particle mean settling velocity and the isolated-particle settling velocity; open circles, the hindered settling velocity predicted by the empirical correlation (3.1).

the particle settling speed: the drag increase related to nonlinear and unsteady drags on the particles in a turbulent environment (Fornari *et al.* 2016*b*). These effects play a more significant role when the turbulence fluctuation is stronger than the particle settling velocity, which can be quantified by the ratio u_0'/V_{s0} (Fornari *et al.* 2016*b*). In other words, the nonlinear and unsteady contributions to the drag decrease in relative value as the settling speed increases in comparison with the turbulence intensity. As a consequence, the difference between $\langle V_s\rangle$ and $\langle V_s\rangle_{hindered}$ is expected to decrease as the ratio V_{s0}/u_0' increases (i.e. with the increasing Galileo number), as confirmed by the data shown in figure 3(*b*).

We further compare the present simulations with previously proposed drag models for settling particles in turbulence. To this end, we define the drag coefficient based on the mean slip velocity between the particle and fluid phases as

$$C_d = \frac{\langle F_d\rangle_p}{\frac{1}{2}\rho_f U_s^2 A}. \tag{3.3}$$

Here, $\langle F_d\rangle_p$ is the particle-averaged drag force and can be related to the buoyancy as $\langle F_d\rangle_p = \pi D^3(\rho_p - \rho_f)g/6$; $U_s = |\langle V_s\rangle - \langle U_f\rangle|$is the mean slip velocity; $A = \pi D^2/4$ is the front area of the particle. Note that the fluid phase has a mean upward velocity $\langle U_f\rangle = -\phi\langle V_s\rangle/(1-\phi)$ (the negative sign indicates the opposite direction to the particle mean settling velocity), which maintains the zero net flux of the whole system by compensating the downward flux of the settling particles (Yin & Koch 2007). From the modelling perspective, Xia *et al.* (2022) proposed the following correlation for the mean drag coefficient based on their PR-DNS of settling particles in an otherwise quiescent fluid (indicated by the subscript '$quie$'):

$$C_{d,quie}^{model} = \frac{24}{Re_m}\left(1 + 0.15Re_m^{0.687}\right)(1-\phi)^{1-n}, \tag{3.4}$$

where the Reynolds number Re_m is defined as $Re_m = (1-\phi)Re_p$ with $Re_p = U_s D/\nu$ the particle Reynolds number based on the mean slip velocity, and the index n given by the

https://doi.org/10.1017/jfm.2026.11476 Published online by Cambridge University Press

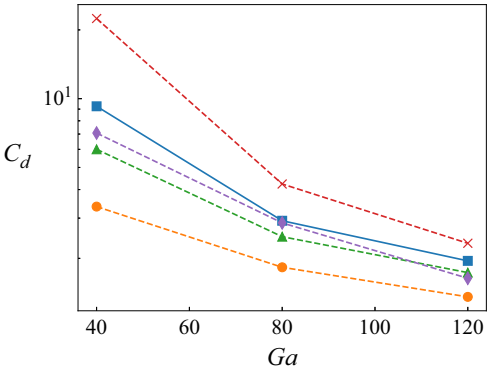


Figure 4. Drag coefficient, (■) present simulation results; (●) hindered settling modelled by (3.1); (▲) the drag model in the otherwise quiescent fluid given by (3.4); (×) the drag model accounting for the background turbulent given by (3.6); (♦) the turbulence-induced settling attenuation predicted by the model (3.9).

empirical formula

$$n = \left[3.88 - 0.38 \ln\left(Re_p\right)\right] \ln\left(\phi^{-1}\right) \left(\rho_p/\rho_f\right)^{-0.038}. \tag{3.5}$$

When further accounting for the background turbulent flows, the drag increase can be modelled by multiplying the drag coefficient with the prefactor $(1 + \psi)$, i.e. (Xia *et al.* 2022)

$$C_{d,turb}^{model} = (1 + \psi) C_{d,quie}^{model}. \tag{3.6}$$

The parameter ψ is given by the empirical expression (Xia *et al.* 2022)

$$\psi = 0.448 \left[\frac{k}{U_s^2} - \left(\frac{k}{U_s^2}\right)_0\right]^{0.525}, \tag{3.7}$$

in which k indicates the turbulent kinetic energy; $(k/U_s^2)_0$ represents the effect of particle-induced turbulent kinetic energy and can be modelled by (Mehrabadi *et al.* 2015)

$$\left(\frac{k}{U_s^2}\right)_0 = \phi + 1.25\phi(1 - \phi)^3 \exp(-\phi Re_m^{1/2}). \tag{3.8}$$

In addition, another simplified model that predicts the settling velocity of heavy particles in HIT was recently proposed by Peng *et al.* (2025),

$$\frac{V_s^{turb}}{V_{s0}} = \frac{k_3}{k_3 + Re_{s0}} \left(1 + \frac{1}{k_2 + S_L}\right) + \frac{Re_{s0}}{k_3 + Re_{s0}} \left(\frac{k_1}{k_1 + D/\eta_0} \frac{1}{S_L} + \frac{D/\eta_0}{k_1 + D/\eta_0} \frac{S_L}{1 + S_L}\right), \tag{3.9}$$

in which V_s^{turb} denotes the settling velocity in a turbulent flow, S_L represents the ratio between the isolated settling velocity and the r.m.s. velocity of the turbulent flow and k_1, k_2, k_3 are fitting parameters that can be simply set to unity (Peng *et al.* 2025). The comparison of the present simulation results with the empirical models introduced above is presented in figure 4. As we can see, ignoring the turbulence effect (hindered settling modelled by (3.1) or (3.4)) leads to an underestimation of the drag coefficient, with the discrepancy reducing with Ga owing to the increase of the ratio between particle settling velocity and the turbulent velocity fluctuations. Nevertheless, the drag coefficient predicted by the (3.4) is superior to the simplified hindrance-settling model given by (3.1). It is surprising that the drag coefficient predicted by the model (3.9) (see the

https://doi.org/10.1017/jfm.2026.11476 Published online by Cambridge University Press

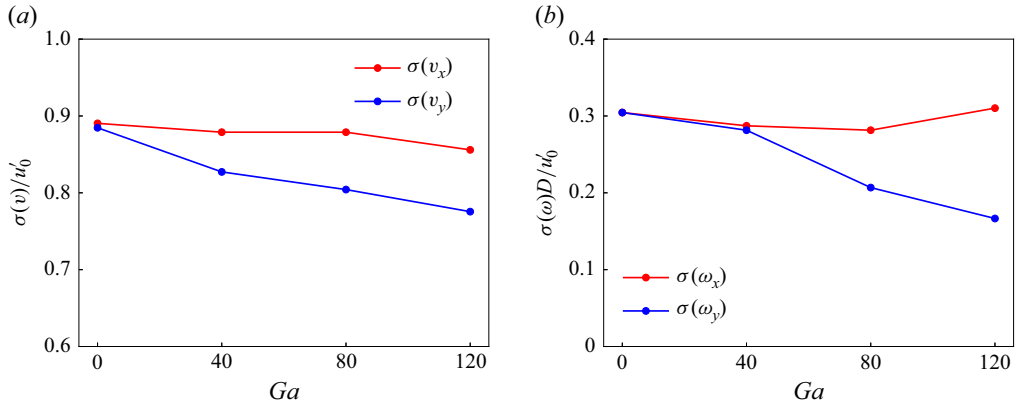


Figure 5. Standard deviations of the (*a*) translational velocity and (*b*) angular velocity of the dispersed particles.

diamonds in figure 4) agrees well with the present simulation results, although the volume fraction effect is not incorporated in this empirical model. Whether this agreement is robust is worthy of further examination since the hindrance effect and the particle-induced turbulence modulation are neglected by this empirical mode, which was mainly assessed at very low volume fractions (Peng *et al.* 2025). Moreover, the model given by (3.6), which accounts for both the hindrance and turbulent effects, overestimates the drag coefficient. This discrepancy may be related to the different flow configuration (vertical channel flows) and different particle properties in the modelling work by Xia *et al.* (2022).

To gain further insights, we examine the fluctuations of the particle motion. Figure 5 displays the standard deviation of the particle linear and angular velocities along the horizontal and vertical directions. As shown in figure 5(*a*), the magnitude of the particle velocity fluctuations is of the same order of that of the fluid phase, indicating the dominance of the turbulent transport on the dynamics of the neutrally (or almost neutrally) buoyant particles under consideration. However, it is noteworthy that the standard deviation of the particle vertical velocity decreases when increasing the Galileo number, while the changes of the horizontal velocity fluctuations are hardly visible. Thus, the fluctuations of the particle motions are weaker along the vertical direction than those in the horizontal direction, i.e. $\sigma(v_y) < \sigma(v_x)$, in agreement with the results by Fornari *et al.* (2016*a*). This is also in contrast to the fluid phase with a greater velocity fluctuations along the gravity direction (see figure 1*b*). Note additionally that the particle velocity fluctuation was found to be higher along the vertical direction for the particle sedimentation in an otherwise quiescent fluid (Fornari *et al.* 2016*a*; Zaidi 2018; Jiang *et al.* 2026).

The larger vertical velocity fluctuations for settling particles in a quiescent fluid were ascribed to the wake-induced hydrodynamic interactions between settling particles. However, with the background turbulence, the turbulent fluctuations disrupt the particle wakes; the particle velocity fluctuations are instead caused mainly by the turbulent eddies in this scenario (Fornari *et al.* 2016*a*). We therefore suggest that the particle settling acts as a filter of the turbulent eddies and thus partially screens the particle motion from the background turbulence. As a consequence, the vertical velocity fluctuations of the dispersed particles decrease with the Galileo numbers. As regards the rotational motion, we observe in figure 5(*b*) that the standard deviation of the angular velocity around the horizontal direction is higher than that around the vertical direction. This observation, in agreement with the case of particle sedimentation in a quiescent fluid (Jiang *et al.* 2026), is explained by the dominant horizontal vorticity in the wakes produced by the settling particles.

https://doi.org/10.1017/jfm.2026.11476 Published online by Cambridge University Press

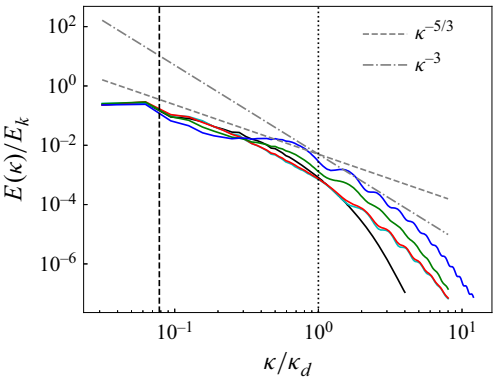


Figure 6. Spherical-shell energy spectra for single-phase flow (black), particle-laden flows at $Ga = 0$ (cyan), $Ga = 40$ (red), $Ga = 80$ (green) and $Ga = 120$ (blue). The energy spectra are normalized by the total kinetic energy $E_k = \sum_{\kappa=0}^{\kappa_{max}} E(\kappa)$. The vertical dashed and dotted lines depict the cutoff wavenumber κ_f and the wavenumber corresponding to the particle scale, $\kappa_d = 2\pi/D$, respectively.

3.3. *Energy spectra and SBS analysis*

In this section, we investigate the turbulence modulation by the presence of dispersed particles in the spectral space. We will first examine the spherical-shell integral of the energy spectra and the corresponding SBS energy budget. Then, we will display the two-dimensional distribution of the spectra in the Fourier space and discuss the anisotropy of the energy budget caused by the particle sedimentation.

3.3.1. *The spherical-shell spectral analysis*

We start with the energy spectrum of the fluid flow. In figure 6 we present the energy spectra of the single-phase and particle-laden turbulent flows as functions of the spherical-shell wavenumber $\kappa = \|\boldsymbol{\kappa}\|$. As we can see, in comparison with the single-phase flow, the energy spectra rise at small scales whereas the energy contained in the large scales is attenuated in the particle-laden turbulent flows, an observation also made in earlier studies on particle-laden turbulence (Wang *et al.* 2014; Bhattacharjee *et al.* 2024). This phenomenon of energy depletion at large scales and reinjection into small scales has been attributed to two main mechanisms (Peng *et al.* 2023): (i) the promotion of energy transfer by particles due to the enhanced dissipation rate in the vicinity of the particle surfaces (Tanaka & Eaton 2010; Botto & Prosperetti 2012); (ii) the enhanced vorticity stretching caused by the particles (Peng *et al.* 2023). As a consequence of the particle-induced energy transfer, a κ^{-3} scaling of the energy spectra is observed in the particle-laden flows, an observation widely reported in the case of bubble/particle-induced pseudoturbulence (Lance & Bataille 1991; Martínez Mercado *et al.* 2010; Pandey *et al.* 2020; Innocenti *et al.* 2021; Jiang *et al.* 2025).

Moreover, we also notice from figure 6 that the pivot wavenumber $\kappa^\bigstar$, the intersection point of the energy spectra of the single-phase and particle-laden flows, is close to the particle scale ($\kappa^\bigstar \approx \kappa_d$) for the case without or with weak particle sedimentation velocity (at $Ga = 0$ or 40), a similar observation also reported in previous studies of particle-laden turbulent flows (Wang *et al.* 2014; Peng *et al.* 2023; Chiarini & Rosti 2024). However, it is noteworthy that the pivot wavenumber $\kappa^\bigstar$ shifts towards lower wavenumbers with the increase of the Galileo number, indicating an enhanced particle-induced turbulence modulation as the particle sedimentation becomes faster. Accordingly, the $\kappa^{-5/3}$ scaling

https://doi.org/10.1017/jfm.2026.11476 Published online by Cambridge University Press

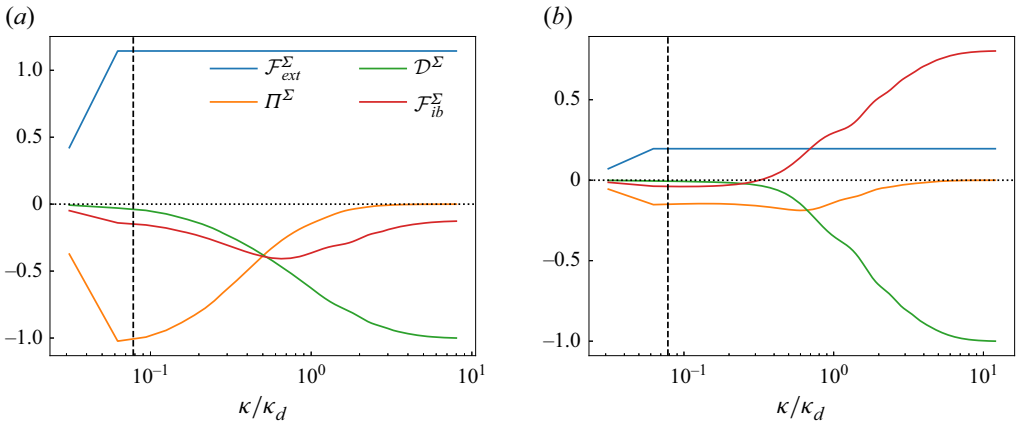


Figure 7. Cumulative SBS energy budget for (*a*) case 1 with $Ga = 0$ and (*b*) case 4 with $Ga = 120$. The total viscous dissipation $\mathcal{D}^{\Sigma}_{tot} = -\sum_{\kappa=0}^{\kappa_{max}} \mathcal{D}(\kappa)$ is used to normalize the data.

of the energy spectrum, which characterizes the classic energy cascade in the inertial range of the single-phase turbulent flow, becomes hardly visible in the suspensions with $Ga = 80$ and 120. Note that a Kolmogorov scaling $\kappa^{-5/3}$ of the energy of bubble-induced turbulence was identified at the sub-bubble scales in the recent experimental work by Ma *et al.* (2025) (these authors report the equivalent $r^{2/3}$ scaling of the second-order structure function, with r being the separation distance) at the high Galileo number of $Ga \sim O(1000)$. We, however, did not observe such a Kolmogorov scaling at small scales in the present study, probably due to the fact that the Galileo number under consideration is not high enough. Whether a similar scaling can be observed in the settling-particle pseudoturbulence is worth future explorations by experiments/simulations of particle-laden flows at high Ga. We also note that the recent numerical work by Chiarini *et al.* (2025) reported a κ^{-4} scaling of the energy spectra for the HIT laden with (non-settling) Kolmogorov-size particles. The turbulence modulation by such small particles with gravity sedimentation also needs further examination.

We now examine the SBS energy budget of the fluid flow in each suspension. We first compare in figure 7 the cumulative spherical-shell SBS energy budget for the flow with no particle settling and with the highest Galileo number under study. The cumulative contribution to the budget, denoted by $\mathcal{J}^{\Sigma}(\kappa)$, is defined as the sum of the spherical-shell spectrum up to the given wavenumber κ, i.e.

$$\mathcal{J}^{\Sigma}(\kappa) = \sum_{\kappa=0}^{\kappa_{max}} \mathcal{J}(\kappa)\,. \tag{3.10}$$

As shown in figure 7(*a*), the external EP forces inject energy into the flow system at the scales larger than that of the cutoff wavenumber κ_f, effectively serving as an energy source; on the other hand, the energy is dissipated by the viscous stresses. The nonlinear interactions transfer energy from large to small scales with zero net energy production/dissipation in the flow (Pope 2000), i.e. $\Pi^{\Sigma} = 0$ at the highest wavenumber.

It is noteworthy that the contribution from the IB forces plays a similar role of transferring energy from large to small scales (indicated by the negative slope of $\Pi^{\Sigma}(\kappa)$ at low wavenumbers and positive slope at high wavenumbers). However, its contribution to the interscale energy transfer is less important than that of the nonlinear effect at small

https://doi.org/10.1017/jfm.2026.11476 Published online by Cambridge University Press

κ, while it directly balances dissipation at large κ. Note additionally that the particle–fluid interactions have a net contribution of energy dissipation (indicated by the negative value of $\mathcal{F}_{ib}^{\Sigma}$ at the highest wavenumber κ_{max}) in the case with $Ga = 0$, a fact which deserves an explanation.

Let us therefore discuss the non-zero energy dissipation due to the particle–fluid interactions. To this end, we resort to the budget of the total fluid kinetic energy $E_k = (u_x^2 + u_y^2 + u_z^2)/2$ in the physical space (see also Chouippe & Uhlmann 2015):

$$\frac{d}{\mathrm{d}t}\langle E_k\rangle_{\Omega} = -\langle\epsilon\rangle_{\Omega} + \left\langle \boldsymbol{f}_{ext}\cdot\boldsymbol{u}\right\rangle_{\Omega} + \left\langle \boldsymbol{f}_{ib}\cdot\boldsymbol{u}\right\rangle_{\Omega}. \tag{3.11}$$

Here, $\langle\cdot\rangle_{\Omega}$ represents the spatial average. The terms on the right-hand side of (3.11) represent the viscous dissipation ($-\langle\epsilon\rangle_{\Omega}$), the energy input by external forces (denoted by $\Psi_{ext} = \left\langle \boldsymbol{f}_{ext}\cdot\boldsymbol{u}\right\rangle_{\Omega}$) and the contribution from the particle–fluid interactions (denoted by $\Psi_p = \left\langle \boldsymbol{f}_{ib}\cdot\boldsymbol{u}\right\rangle_{\Omega}$). These terms are related to the energy budget terms in the spectral space by

$$\langle\epsilon\rangle_{\Omega} = -\sum_{\boldsymbol{\kappa}}\mathcal{D}(\boldsymbol{\kappa}), \quad \Psi_{ext} = \left\langle \boldsymbol{f}_{ext}\cdot\boldsymbol{u}\right\rangle_{\Omega} = \sum_{\boldsymbol{\kappa}}\mathcal{F}_{ext}(\boldsymbol{\kappa}), \quad \Psi_p = \left\langle \boldsymbol{f}_{ib}\cdot\boldsymbol{u}\right\rangle_{\Omega} = \sum_{\boldsymbol{\kappa}}\mathcal{F}_{ib}(\boldsymbol{\kappa}). \tag{3.12}$$

Considering the particle energy budget, the term Ψ_p can be related to the particle motions as follows:

$$\begin{aligned}\Psi_p \approx &\underbrace{-\frac{\phi}{\rho_p V_p}\left(\frac{\rho_p}{\rho_f}-1\right)\left[\rho_p V_p \frac{d}{\mathrm{d}t}\left\langle\frac{1}{2}\boldsymbol{v}\cdot\boldsymbol{v}\right\rangle_p + I_p\frac{d}{\mathrm{d}t}\left\langle\frac{1}{2}\boldsymbol{\omega}\cdot\boldsymbol{\omega}\right\rangle_p\right]}_{\Psi_p^{acc}} + \underbrace{\phi\left(\frac{\rho_p}{\rho_f}-1\right)\langle\boldsymbol{v}\rangle_p\cdot\boldsymbol{g}}_{\Psi_p^{gra}} \\ &+ \underbrace{\frac{\phi}{\rho_f V_p}\left[\langle\boldsymbol{v}\cdot\boldsymbol{F}_C\rangle_p + \langle\boldsymbol{\omega}\cdot\boldsymbol{T}_C\rangle_p\right]}_{\Psi_p^{col}} \underbrace{-\frac{\phi}{V_p}\left\langle\boldsymbol{v}\cdot\int_{\Omega_p}\boldsymbol{f}_{ext}\mathrm{d}V + \boldsymbol{\omega}\cdot\int_{\Omega_p}\boldsymbol{r}\times\boldsymbol{f}_{ext}\mathrm{d}V\right\rangle_p}_{\Psi_p^{ext}}.\end{aligned} \tag{3.13}$$

The derivation of the above equation, which was originally performed in Chouippe & Uhlmann (2015), is provided in Appendix A for completeness. According to (3.13), the total work related to the particle–fluid interactions Ψ_p is composed of the contributions from the particle acceleration Ψ_p^{acc}, the particle sedimentation Ψ_p^{gra}, interparticle collisions Ψ_p^{col} and the term related to the external forces Ψ_p^{ext}. Note that the term inside the square bracket of Ψ_p^{acc} can be reformulated as

$$\rho_p V_p \frac{d}{\mathrm{d}t}\left\langle\frac{1}{2}\boldsymbol{v}\cdot\boldsymbol{v}\right\rangle_p + I_p\frac{d}{\mathrm{d}t}\left\langle\frac{1}{2}\boldsymbol{\omega}_p\cdot\boldsymbol{\omega}_p\right\rangle_p = \frac{1}{2}\frac{d}{\mathrm{d}t}\left\langle\rho_p V_p\boldsymbol{v}^2 + I_p\boldsymbol{\omega}^2\right\rangle_p, \tag{3.14}$$

namely the time derivative of the particle-averaged kinetic energy. Hence, Ψ_p^{acc} can only have a non-zero contribution to the energy budget for a non-equilibrium flow; for example, it works either as a energy source or sink, depending on the particle size, in particle-laden decaying turbulence (Lucci *et al.* 2010). In the steady state of sustained turbulence, however, Ψ_p^{acc} is equal to zero. Additionally, Ψ_p^{gra} is equal to zero when the particles do not settle ($Ga = 0$). As regards the other two terms in (3.13), the contribution from particle–particle collisions was reported to be negligible at the volume fraction $\phi \sim O(0.1)$ (Chiarini & Rosti 2024), which is also confirmed in the present simulations.

https://doi.org/10.1017/jfm.2026.11476 Published online by Cambridge University Press

Hence, from our simulation results, the last term Ψ_p^{ext} is mainly responsible for the negative value of Ψ_p in the case of $Ga = 0$, corresponding to a weak but non-negligible net energy dissipation associated with the particle–fluid interactions (see figure 7*a*).

As shown in Appendix B, the net dissipation originated from the IB forces at $Ga = 0$ is related to the non-zero EP external forces applied also inside the rigid particles. However, as shown in the same appendix, this contribution becomes almost negligible when the external forcing is excluded from the solid region; then the residual contribution is merely from interparticle collisions (Ψ_p^{col}). Note, also, from the definition of Ψ_p^{ext} that a negative value of this term indicates a positive correlation between the particle velocities and the external forces sustaining the turbulence, which is attributed to the tendency of neutrally buoyant particles to follow local fluid flows produced by the external forces. Although it might have been preferable to force the turbulence only in the fluid phase, we show that this does not change the physics discussed in this work, especially above the wavenumbers of the external forcing, which acts at the large scale of the computational domain.

Now let us move back to the discussion on figure 7(*b*), which provides the cumulative SBS budget of the fluid kinetic energy in the suspension with $Ga = 120$. Compared with the non-sedimentation case ($Ga = 0$ in figure 7*a*), it is obvious that the total work done by the IB forces is significantly augmented. The positive value of $\mathcal{F}_{ib}^{\Sigma}(\kappa_{max})$ indicates a net energy input by the particle–fluid interactions at $Ga = 120$. This is because the contribution from the particle sedimentation, i.e. Ψ_p^{gra} in (3.13), does positive work in the flow system, which overwhelms the energy dissipation caused by collisions and external forces inside the particles (negative values of Ψ_p^{col} and Ψ_p^{ext}); the work done by the settling particles, instead of the energy production by the external EP forces, serves as the major source of the energy input. As a consequence, to close the energy budget, the viscous dissipation becomes greater than Ψ_{ext}, different from the physics in the single-phase turbulence.

To have a clearer comparison between different cases, we show the cumulative contributions to the energy budget in figure 8: in particular, we display the nonlinear transfer Π^{Σ}, viscous dissipation $\mathcal{D}^{\Sigma}$ and the particle–fluid interactions $\mathcal{F}_{ib}^{\Sigma}$ at different Ga. These comparisons illustrate the modulation of the energy budget in the particle-laden turbulence with varying particle settling velocity. We first observe from figure 8(*a*) that the total energy input by the IB forces, i.e. the value of $\mathcal{F}_{ib}^{\Sigma}$ at the highest wavenumber, increases monotonically with the Galileo number. This enables us to provide an estimate of the ratio between the energy input by the gravity sedimentation and the external forces that sustain the single-phase turbulence:

$$\Lambda = \frac{\Psi_p^{gra}}{\Psi_{ext}} \approx \frac{\Psi_p^{gra}}{\epsilon_0} = \frac{\phi\left(\rho_p/\rho_f - 1\right) g \langle V_s \rangle}{\epsilon_0} = \frac{\phi Ga^2 Re_s}{5832\epsilon_0^*}. \tag{3.15}$$

Here, $Re_s = \langle V_s \rangle D/\nu$ is the Reynolds number based on the particle mean settling velocity $\langle V_s \rangle$, and $\epsilon_0^* = \epsilon \tau_p^3/D^2$ is the dimensionless viscous dissipation of the single-phase turbulence provided in table 2. Note that we use the single-phase viscous dissipation ϵ_0 to estimate the energy production by the external forces Ψ_{ext}, which is only strictly valid for the single-phase flow. However, the difference between ϵ_0 and Ψ_{ext} is also found to be small (up to approximately 10 %) in the particle-laden cases under consideration. As the dimension of the particle is an order of magnitude smaller than the energy-input scale (i.e. $\kappa_d/\kappa_f = 12.8 \gg 1$), the energy input by the large-scale external forces is not significantly affected by the presence of particles.

In table 4 we list the value of Λ computed by (3.15) with the mean particle settling velocity obtained from the simulations. Not surprisingly, Λ increases with the Galileo

https://doi.org/10.1017/jfm.2026.11476 Published online by Cambridge University Press

Case	Ga	Re_s	Λ
1	0	0	0
2	40	13.7	0.07
3	80	48.7	0.94
4	120	89.3	3.92

Table 4. Ratio Λ between the energy input by the particle settling and by the external forces maintaining turbulence for the different cases under examination. See text for the definition of Λ in (3.15).

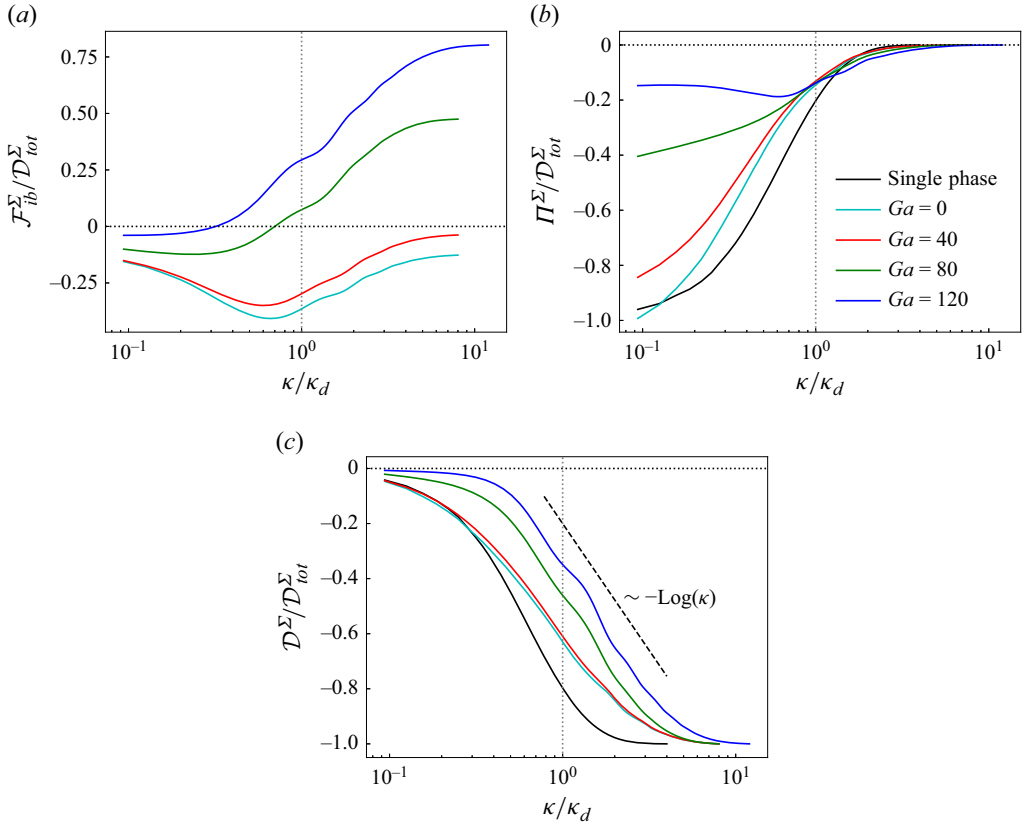


Figure 8. Comparison of the cumulative contributions to the SBS energy budget for the different Galileo number under consideration: (*a*) IBM forcing term; (*b*) nonlinear transfer; (*c*) viscous dissipation. Here we only present the data for $\kappa > \kappa_f$.

number because of the increased particle settling velocity. Also, it is noteworthy that the ratio is as low as $\Lambda = 0.07$ for the case with $Ga = 40$, indicating the negligible energy input by gravity sedimentation compared with the external forces. This is in agreement with the marginal difference regarding the SBS budgets between the cases with $Ga = 0$ and $Ga = 40$ (the red and cyan lines in figure 8). Nevertheless, increasing the Galileo number to $Ga = 80$, the energy injection due to the particle sedimentation becomes comparable to that of the external forces with $\Lambda = 0.94$; the former contribution becomes the predominant mechanism of energy production at $Ga = 120$ when the contribution from the particle sedimentation exceeds the EP forces by a factor approximately 4 ($\Lambda = 3.92$).

https://doi.org/10.1017/jfm.2026.11476 Published online by Cambridge University Press

We also observe from figure 8(*a*) that the large-scale energy transfer by the particle–fluid interactions, indicated by the negative slope of $\mathcal{F}_{ib}^{\Sigma}(\kappa)$ in the suspensions with $Ga = 0$ and 40, becomes negligible at higher Galileo numbers. As discussed below, the decrease with Ga of the net energy removal by the settling particles at large scales is associated with a cancellation between the additional injection of energy into vertically elongated scales and the quenching of the horizontal flow correlations, so at the origin of the flow anisotropy. Furthermore, the range of scales on which the energy is injected by the particle–fluid interactions (region with positive slope of $\mathcal{F}_{ib}^{\Sigma}(\kappa)$) is enlarged when increasing the Galileo number.

The different behaviour of the particle–fluid interactions also alters the energy transport by the nonlinear terms. As shown in figure 8(*b*), this energy transfer is weakened as the Galileo number increases. For the greatest particle settling velocity at $Ga = 120$, the contribution from the nonlinear transfer to the energy budget becomes subdominant compared with those from the particle–fluid interaction and the viscous dissipation (see figure 7*b*). In other words, the energy input by the particle sedimentation is almost in direct balance with the viscous dissipation within a wide wavenumber range, i.e. $\mathcal{F}_{ib}(\kappa) \approx -\mathcal{D}_{ib}(\kappa)$, at $Ga = 120$. This observation supports the local-balance assumption proposed by Lance & Bataille (1991) regarding the pseudoturbulence induced by rising bubbles. In our recent study on the particle sedimentation in an initially quiescent fluid (Jiang *et al.* 2025), we also observed this local balance in the particle-induced pseudoturbulence, which leads to the κ^{-3} scaling of the energy spectra. Note, however, that this local balance is only observed at the smallest scales at lower Ga.

As regards the spherical-shell spectra of the viscous dissipation, we observe from figure 8(*c*) that $\mathcal{D}^{\Sigma}(\kappa) \sim -\log(\kappa)$ on the scales close to the particle size, corresponding to the $E(\kappa) \sim \mathcal{D}(\kappa)/\kappa^2 \sim \kappa^{-3}$ scaling of the energy spectra for the particle-laden flows shown in figure 6. Note, interestingly, that this scaling is not clearly observed in the particle-laden turbulence with $Ga \leqslant 40$ (in absence of or with weak gravity sedimentation), when the local-balance mechanism only holds at the smallest scales.

To gain more insights on the small-scale dynamics, we further examine the energy budget at scales smaller than the particle size. Specifically, we compute the integrals of the nonlinear transfer term, IB forcing term and the viscous dissipation term at $\kappa \geqslant \kappa_d$, denoted by

$$\Pi^{<} = \sum_{\kappa \geqslant \kappa_d} \Pi(\kappa), \quad \mathcal{F}_{ib}^{<} = \sum_{\kappa \geqslant \kappa_d} \mathcal{F}_{ib}(\kappa), \quad \mathcal{D}^{<} = \sum_{\kappa \geqslant \kappa_d} \mathcal{D}(\kappa). \tag{3.16}$$

The physical interpretations of these three quantities are: (i) $\Pi^{<}$ the total nonlinear energy transfer by inertia from larger scales to subparticle scales; (ii) $\mathcal{F}_{ib}^{<}$ the total energy contribution from the particle–fluid interactions at subparticle scales; (iii) $\mathcal{D}^{<}$ the total energy dissipation at subparticle scales. The values of $\Pi_{ib}^{<}$, $\mathcal{F}_{ib}^{<}$ and $\mathcal{D}^{<}$ are shown in figure 9 for all cases being examined, normalized by the single-phase dissipation rate ϵ_0. Note first that the balance of the energy budget suggests $\mathcal{D}^{<} = -(\Pi^{<} + \mathcal{F}_{ib}^{<})$, which is confirmed by the data shown in figure 9. In contrast to the single-phase turbulence with only the nonlinear transfer as energy source, the particle–fluid interaction always provides a net energy input at subparticle scales in the particle-laden cases. In other words, the IB forces do positive work at small scales, regardless of the Galileo number. As the Galileo number increases, the energy input by particle sedimentation is enhanced due to the greater particle settling velocity; the energy brought to small scales by nonlinear effects decreases in particle-laden flows with $Ga \leqslant 40$ and then increases, remaining, however, lower than the input by the sedimentation at high $Ga \geqslant 80$. It is also interesting to note that the

https://doi.org/10.1017/jfm.2026.11476 Published online by Cambridge University Press

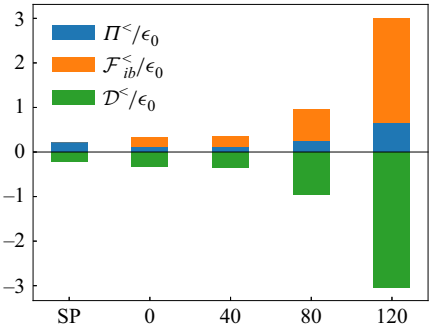


Figure 9. The energy budget at small scales (smaller than the particle size, $\kappa \geqslant \kappa_d$) for the different suspension flows under investigation. The numbers on the horizontal axis represent the Galileo number, except for 'SP' standing for the single-phase turbulence.

absolute value of $\Pi^<$ is larger than that of the single-phase turbulence at $Ga = 120$. This indicates that the energy injection by the particle–fluid interaction, which starts at scales larger than the particle size (see the positive slope of $\mathcal{F}^{\Sigma}_{ib}$ at $\kappa \lesssim \kappa_d$ in figure 8*a*), would be partially transferred to small scales by inertial effects. The results shown in figures 8 and 9 suggest that more energy is available at $\kappa = \kappa_d$ at high Ga, which is sufficient to trigger nonlinear velocity fluctuations and to force an extension of the dissipative range towards smaller scales.

The analysis of the SBS budget indicates how the combined effects of the particle-enhanced energy cascade (evident at $Ga = 0$ or 40) and the energy input by particle sedimentation (more evident at $Ga = 80$ or 120) alter the energy transfer path in the particle-laden turbulent flows. In particular, the energy transfer induced by the particle–fluid interactions quenches the classic inertia-driven energy cascade (characterized by $E(\kappa) \sim \kappa^{-5/3}$ in the inertial range), leading to a robust κ^{-3} scaling of the energy spectra. When settling is null or relatively weak, the local balance between fluid–structure interactions and dissipation is seen only at small scales. As soon as the settling speed (or equivalently the Galileo number) increases, the κ^{-3} scaling of the energy spectra appears on wider scale ranges, even at the largest flow scales, completely masking the classic $\kappa^{-5/3}$ spectra for the highest Ga under the current investigation. Indeed, we notice the coexistence of the $\kappa^{-5/3}$ and κ^{-3} scalings of the energy spectra at different scales in the suspensions with $Ga = 0$ and $Ga = 40$ (see the cyan and red lines in figure 6); in these flows, the modulation of the energy transfer by the particle–fluid interactions does not reach the inertial scales and remains limited to structures smaller than the particle size. A similar observation regarding the coexistence of inertia-dominated and fluid–structure-dominated dynamics underlying the energy spectrum was also reported in bubble-laden and particle-laden turbulent flows (Pandey, Mitra & Perlekar 2023; Chiarini & Rosti 2024).

3.3.2. *The spectral analysis on the two-dimensional plane*

To further understand the directional information of the turbulence modulated by the settling particles, we analyse the energy budget on the two-dimensional $\kappa_h - \kappa_y$ plane, corresponding to horizontal and vertical wavenumbers. First, we present in figure 10 the two-dimensional distribution of the energy spectral density. Here, we display the data with linear scale in figure 10(*a–d*) to better illustrate the isotropy/anisotropy and with log scale on the bottom row to clarify the large-scale information. In each panel, we display with dashed lines the results pertaining to the suspension with $Ga = 0$.

https://doi.org/10.1017/jfm.2026.11476 Published online by Cambridge University Press

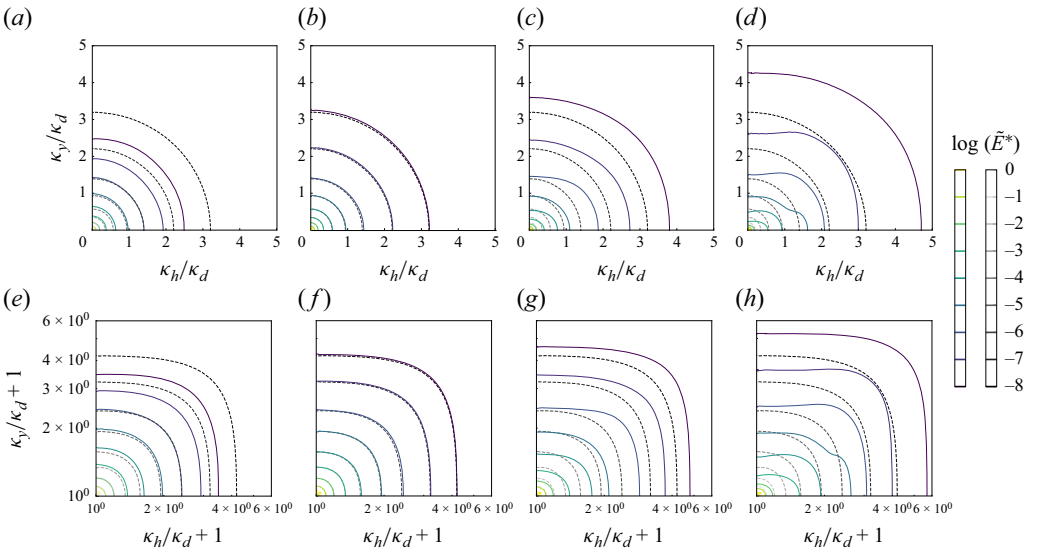


Figure 10. Energy spectral density in the $\kappa_h - \kappa_y$ plane. The notation $\tilde{E}^*$ denotes the normalized energy spectral density, i.e. $\tilde{E}^* = \tilde{E}/(E_k D^3)$. The dashed grey contour lines depict the result for the particle-laden turbulence without particle sedimentation ($Ga = 0$), while the coloured solid lines illustrate the result for (*a*,*e*) the single-phase flow, and the particle-laden flows with (*b*,*f*) $Ga = 40$, (*c*,*g*) $Ga = 80$ and (*d*,*h*) $Ga = 120$. The linear scale is used for the axes in (*a–d*) while the log scale is used in (*e–h*).

Figure 10(*a*,*e*) compare the single-phase turbulence with the particle-laden flow of neutrally buoyant particles. As expected, the energy distribution retains isotropy in the absence of particle sedimentation, as shown by the concentric-circle contour lines of $\tilde{E}^*$ with the linear scale of κ_h and κ_y (figure 10*a*), or the diagonal-symmetric contour lines with the log-scale axes (figure 10*e*). The presence of particles induces a slower decay of $\tilde{E}^*$ along the radial direction, i.e. an increase of energy at the smallest scales, which is in agreement with the raised spherical-shell energy spectrum below the particle scale shown in figure 6.

For the cases with non-zero Galileo numbers, we observe from figure 10(*b–d*,*f–h*) that the particle sedimentation breaks the isotropy of the energy distribution in the spectral space. The contour lines of $\tilde{E}^*$ are elongated along the κ_h-direction on the scales close to or moderately smaller than the particle size ($\kappa_h \gtrsim \kappa_d$), an observation becoming more prominent as the Galileo number increases. Specifically, for a given solid contour line at intermediate scales in figures 10(*c*) or 10(*d*), which represents flow structures with equal energy, we see that its intercept on the horizontal axis occurs at larger wavenumber than that on the vertical axis. This indicates the larger physical dimension of this flow structure along the vertical direction than the horizontal, and can be related to the local flow structures around the settling particles: thin shear layers and elongated wakes appear in the lateral and vertical directions, respectively (see also Fornari *et al.* 2016*a*). Note, however, that the contour lines of $\tilde{E}^*$ tend to recover symmetry far from the origin of the $\kappa_h - \kappa_y$ plane, indicating the recovery of the flow isotropy at small scales. As concerns the suspension at $Ga = 40$, however, the anisotropy is hardly visible (figure 10*b*,*f*). This can be ascribed to the marginal effect of particle sedimentation as the particle mean settling velocity is significantly smaller than the turbulent velocity fluctuations ($\langle V_s \rangle / u' = 0.21$) in this case.

https://doi.org/10.1017/jfm.2026.11476 Published online by Cambridge University Press

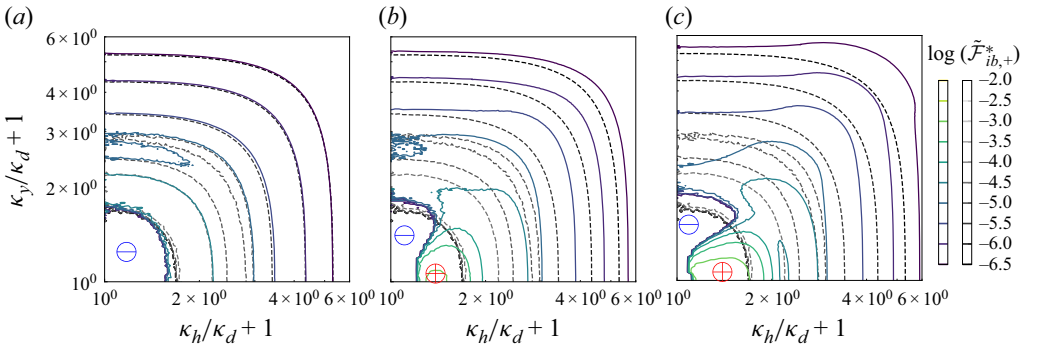


Figure 11. Spectra of the IB forcing work in the $\kappa_h-\kappa_y$ plane for the particle-laden flows under investigation. The data is normalized by $\tilde{\mathcal{F}}^*_{ib}=\tilde{\mathcal{F}}_{ib}/(\mathcal{D}^{\Sigma}_{tot}D^3)$, and only positive values of $\tilde{\mathcal{F}}^*_{ib}$ are illustrated by contour lines (denoted by the subscript '+') . The dashed grey lines correspond to non-settling particles ($Ga=0$), while the coloured solid lines illustrate the results for (*a*) $Ga=40$, (*b*) $Ga=80$ and (*c*) $Ga=120$. Log-scale axes are used. The symbols $\oplus$ and $\ominus$ indicates the region with negative values of $\tilde{\mathcal{F}}^*_{ib}$ and the position of the positive peak of $\tilde{\mathcal{F}}^*_{ib}$.

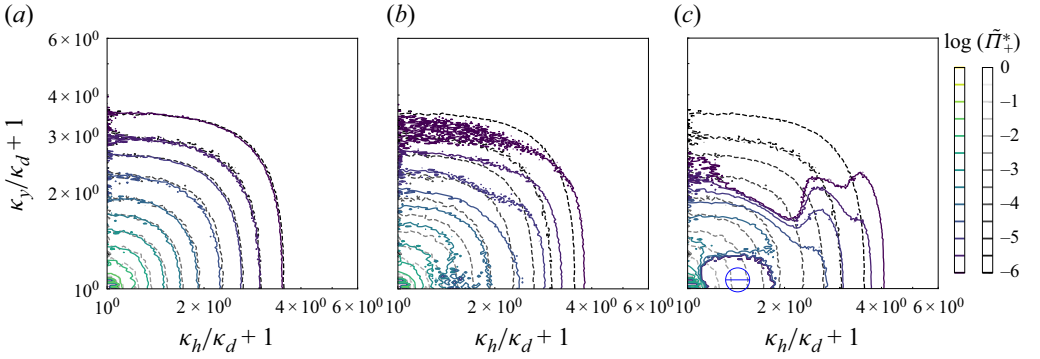


Figure 12. Same as figure 11 but for the two-dimensional spectra of the nonlinear term $\tilde{\Pi}$.

Next, we present the two-dimensional contours of the spectral density associated with the IB forcing in figure 11 and with the nonlinear term in figure 12. In each panel, the results pertaining to a non-zero settling velocity are compared with the case of $Ga=0$. As shown in figure 11(*a*) with the results at $Ga=0$ and 40, the particle–fluid interactions mainly transfer energy from large to small scales along the radial direction in the spectral space so the flow anisotropy is hardly visible; in particular, the directional bias of $\tilde{\mathcal{F}}_{ib}$ is null for the case with $Ga=0$ and very weak for $Ga=40$. However, when the effect of particle sedimentation becomes significant with the increase of Ga to 80 and 120, we observe a clear positive peak of $\tilde{\mathcal{F}}_{ib}$ around $\kappa_h\approx0.3-0.6\kappa_d$ for low values of κ_y, indicated by the symbol $\oplus$ in figure 11(*b*,*c*), a signature of the energy injection by the settling particles. We therefore demonstrate that the energy input by the gravitational sedimentation is anisotropic in the spectral space, unlike the isotropic large-scale energy injection by the external EP forces. This mechanism is responsible for the anisotropic energy distribution shown in figure 10(*c*,*d*,*g*,*h*). Note also that, the region of the spectral space characterized by negative values of $\tilde{\mathcal{F}}_{ib}$ (marked by $\ominus$ in figure 11), indicating energy removal by the particle–fluid interactions, loses its isotropy at large scales as Ga

https://doi.org/10.1017/jfm.2026.11476 Published online by Cambridge University Press

increases. This is associated with the aforementioned positive peak of $\tilde{\mathcal{F}}_{ib}$ as well. The increased energy injection by particle sedimentation partially cancels out the particle-induced energy transfer from large to small scales, which leads to a decreased energy removal by the IB forces at low wavenumbers (see figure 8*a*). Additionally, the anisotropic energy input by the particle sedimentation becomes more pronounced for higher Ga, along with the positive value of $\tilde{\mathcal{F}}_{ib}$ expanding to lower wavenumbers. To sum up, the settling particles induce flow anisotropy by forcing vertically elongated structures while breaking the flow coherence in the horizontal direction; this only leads to the weakened energy injection/removal at large scales when examining the spherical-shell energy spectra, yet leaves an imprinting on the flow (its anisotropy).

To conclude this section, let us elaborate on the two-dimensional spectrum of the energy transfer by nonlinear terms, with the results shown in figure 12. Similar to figure 10(*a*,*e*) and figure 11(*a*), the two-dimensional plot of $\tilde{\Pi}$ retains isotropy on the $\kappa_h - \kappa_y$ plane for the particle-laden flows with $Ga = 0$ and $Ga = 40$ (figure 12*a*). Increasing the particle settling speed, $\tilde{\Pi}$ exhibits anisotropy in the cases at $Ga = 80$ and 120 (figures 12*b* and 12*c*), which can be seen as a consequence of the anisotropic energy input by the particle–fluid interactions (the IB forcing term).

It is interesting to note the negative peak of $\tilde{\Pi}$ on the horizontal axis at $\kappa_h \approx 0.5\kappa_d$ for the $Ga = 120$ case, highlighted by the symbol $\ominus$ in figure 12(*c*). This indicates the removal of energy by the nonlinear effect at these intermediate scale, as also indicated by the negative slope of $\Pi^{\Sigma}(\kappa)$ for the associated case at $\kappa \approx 0.3\kappa_d - 0.5\kappa_d$ in figure 8(*b*). Notice also that the location of the negative peak of $\tilde{\Pi}$ in figure 12(*c*) coincides with the positive peak of $\tilde{\mathcal{F}}_{ib}$ shown in figure 11(*c*). Therefore, for the flow with a substantial energy supply from the particle sedimentation, part of the energy input by the particle–fluid interaction is transferred outwards at intermediate scales by the nonlinear effects. This is analogy to the energy extraction by inertial effects at large scales for the single-phase turbulence.

3.4. *Particle clustering and collision rate*

3.4.1. *Voronoi analysis*

In this section, we examine the spatial clustering and collision rate of the dispersed particles in the turbulent flows. To begin with, we employ the Voronoi analysis to investigate the particle spatial distribution (Monchaux, Bourgoin & Cartellier 2010). With this analysis tool, the domain is partitioned into Voronoi tessellations of the same number of particles, such that any point in one tessellation is closest to the associated particle. In figure 13(*a*) we present the probability distribution of the volumes of the Voronoi tessellations in each particle-laden case under study. The symbol $\overline{V}_{Voro}$ denotes the Voronoi volume V_{Voro} normalized by the mean value for the same particle concentration, $\langle V_{Voro}\rangle = V_{\Omega}/N_p$. Note that we also show the data for the randomly distributed non-overlapping particles at the same volume fraction $\phi = 10\,\%$ for the sake of comparison. The statistics for the randomly distributed particles are collected by repeatedly generating non-overlapping particles with a Poisson process (Uhlmann 2020). The data in the figure reveal that the PDF of $\overline{V}_{Voro}$ is more intermittent in HIT than for the random spatial distribution, indicating the occurrence of particle clustering (Monchaux *et al.* 2010).

To quantify the degree of particle clustering, we compute the standard deviation of the normalized Voronoi volumes, $\sigma(\overline{V}_{Voro})$, and define the clustering indicator C as the ratio $\sigma(\overline{V}_{Voro})$ to that of the randomly distributed particles (Tagawa *et al.* 2013):

$$C = \sigma(\overline{V}_{Voro})/\sigma(\overline{V}^{rand}_{Voro}). \tag{3.17}$$

https://doi.org/10.1017/jfm.2026.11476 Published online by Cambridge University Press

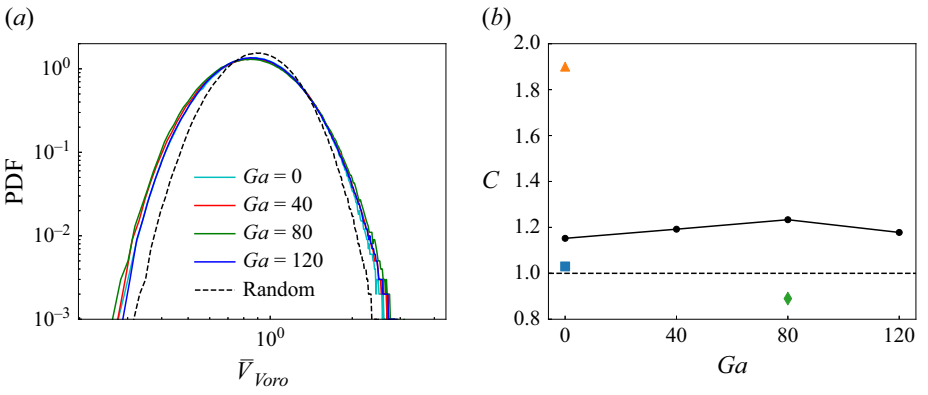


Figure 13. (*a*) Probability density function (PDF) of the normalized Voronoi volumes of the dispersed particles. (*b*) The clustering indicator C versus the Galileo number Ga. The present results (indicated by •) are compared with previous studies, (■) heavy particles in HIT ($\rho_p/\rho_f = 1.5$, $D/\eta = 11$, $\phi = 0.5$ %) (Uhlmann & Chouippe 2017); (▲) heavy particles in HIT ($\rho_p/\rho_f = 1.29$, $D/\eta = 16$, $\phi = 7.9$ %) (Chiarini & Rosti 2024); (⧫) settling particles in the otherwise quiescent fluid ($\rho_p/\rho_f = 2$, $\phi = 5$ %) (Jiang *et al.* 2026).

As shown in figure 13(*b*), the value of C is greater than unity in each case but does not change much with the Galileo number, which is consistent with the PDFs shown in figure 13(*a*). In previous studies, heavy, finite-size particles (without sedimentation) were reported to exhibit clustering in HIT (Fiabane *et al.* 2012; Uhlmann & Chouippe 2017; Chiarini & Rosti 2024), unlike neutrally buoyant particles (Fiabane *et al.* 2012). Nevertheless, particles settling in an otherwise quiescent fluid (without background turbulence) were not observed to cluster in both dilute and non-dilute suspensions at $Ga = 80$ (Jiang *et al.* 2025, 2026). Therefore, turbulence transport, instead of particle sedimentation, plays an essential role in the clustering of finite-size particles; the so-called 'sweep-stick' mechanism (Goto & Vassilicos 2008), i.e. particles preferentially accumulate in weak-fluid-acceleration regions (sticky points), is considered responsible for the particle clustering in most scenarios (Uhlmann & Chouippe 2017; Chiarini & Rosti 2024). This may explain the weak variation of the particle clustering intensity with the particle settling velocity, as shown by the data presented in figure 13(*b*). Moreover, in figure 13(*b*) we also quantitatively compare the clustering indicator from the present data with earlier studies. The discrepancy suggests the sophisticated dependence of the particle clustering on the particle properties, in agreement with the conclusion in Chiarini & Rosti (2024). In particular, the effect of particle sedimentation on the clustering of finite-size particles in HIT remains to be further explored. Note, additionally, that the clustering was found to contribute to the enhancement of particle settling (or bubble rising) velocity in dilute scenarios (Jiang *et al.* 2024*b*; Hessenkemper *et al.* 2025). This effect appears to be negligible in the present set-up given the relatively high-volume fraction; the particle mean settling velocity is always lower than that of an isolated particle as discussed in § 3.2.

3.4.2. *Collision kernel and the particle pair statistics*

Another issue we are concerned with is the collision rate of the dispersed particles, which is relevant to a variety of physical processes in environmental and industrial applications (Pumir & Wilkinson 2016). In a variety of existing studies, the collision kernel Γ is employed to quantify the collision rate in a particulate system (Smoluchowski 1917; Saffman & Turner 1956; Pumir & Wilkinson 2016; Wang 2023). For the monodisperse system, the collision kernel is defined as the rate of collision events normalized by the

https://doi.org/10.1017/jfm.2026.11476 Published online by Cambridge University Press

Ga	0	40	80	120
$\Gamma/(V_{s0}D^2)$	—	3.52	1.38	0.90

Table 5. Collision kernel normalized by the single-particle settling velocity.

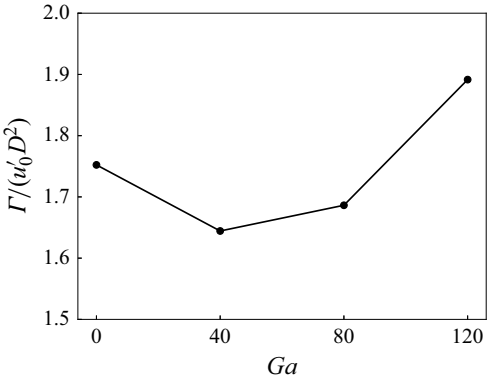


Figure 14. Collision kernel normalized by the r.m.s. velocity fluctuation of the single-phase turbulence as a function of Ga.

square of the particle number density (Wang, Wexler & Zhou 2000),

$$\Gamma = 2\dot{N}_C/n^2. \tag{3.18}$$

Here, $\dot{N}_C$ denotes the number of collision events per unit volume and per unit time, and $n = N_p/V_\Omega$ is the particle number density. To obtain Γ, we count the number of collision events within the statistically steady state during the simulations and then compute the collision kernel by its definition (3.18). As shown in figure 14, the collision kernel Γ, normalized by the single-phase r.m.s. velocity u_0', first decreases slightly with the introduction of particle sedimentation at $Ga = 40$, and then increases when further increasing Ga.

To better examine the combined effect of sedimentation and turbulent transport on the collision rate, we compare the present results with the particle collision kernel in the absence of background turbulence. In our previous study on the particle sedimentation in an initially quiescent fluid (Jiang *et al.* 2026), the collision kernel, normalized by the single-particle settling velocity, was found to be $\Gamma/(V_{s0}D^2) = 0.29$ at $Ga = 80$ – a value obtained at a volume fraction $\phi = 5\,\%$ but found to be insensitive to the particle volume fraction. If we similarly normalize the collision kernels by V_{s0} for the present cases, we can obtain the results of $\Gamma/(V_{s0}D^2)$ as listed in table 5. For the same $Ga = 80$ the collision kernel is increased by approximately 4.75 times in the present turbulent flow when compared with that in the quiescent fluid (Jiang *et al.* 2026). Additionally, the value of $\Gamma/(V_{s0}D^2)$ decreases considerably as Ga increases due to the increase of V_{s0}, which is in contrast to the weak variation of $\Gamma/(u_0'D^2)$ with Ga. Thus, we can conclude that the turbulent transport is the dominant effect for particle collisions in the present flow configuration.

Finally, we attempt to interpret the variations in the collision kernel with the Galileo number shown in figure 14. To this end, we introduce the kinematic description of the

https://doi.org/10.1017/jfm.2026.11476 Published online by Cambridge University Press

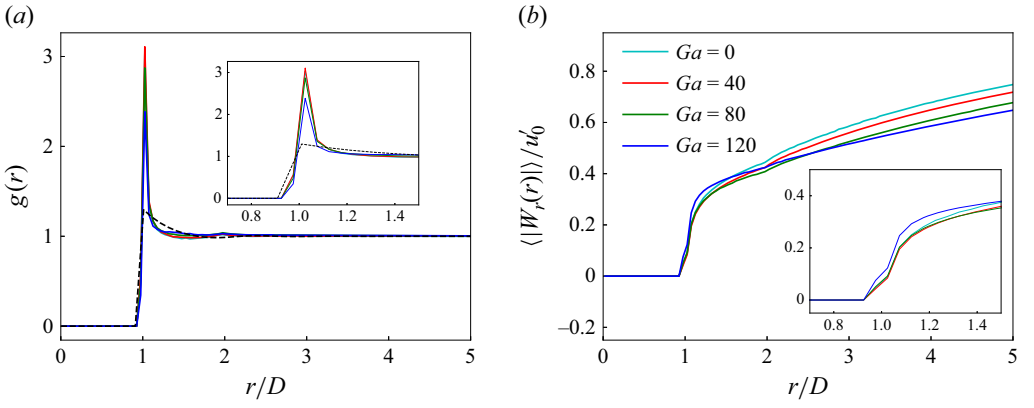


Figure 15. (*a*) Radial distribution function (RDF) and (*b*) relative radial velocity (RRV) of the dispersed particles as function of the separation distance r. The inset panels are the zoom-in view close to $r = D$. The RDF of randomly distributed non-overlapping particles (the hard-sphere distribution, see Liu (2024)) is displayed in panel (*a*) with dashed line for comparison.

collision kernel (Wang *et al.* 2000; Wang 2023),

$$\Gamma^K = 2\pi R^2 \langle |W_r(R)| \rangle g(R). \tag{3.19}$$

Here, $R = D$ is the collision radius, and $\langle |W_r(R)| \rangle$ and $g(R)$ represent the mean absolute RRV and the RDF for particles at the separation distance $r = R$. Readers can refer to Wang *et al.* (2000) for the definitions of RRV and RDF presented in (3.19). To provide a physical interpretation, the kinematic collision Γ^K is the flux of particles across a collision sphere centred at the reference particle with a collision radius $R = D$. The RRV provides the information of the relative motion among particles, whereas the RDF reflects the particle spatial distribution by measuring the probability of finding particles pairs with a given separation distance. Theoretically, the kinematic collision kernel Γ^K is equivalent to the dynamic collision kernel Γ defined in (3.18) (Wang *et al.* 2000).

In figure 15, we display the RDF and RRV as functions of the particle separation distance r. As shown in figure 15(*a*), the RDF exhibits a pronounced peak at $r = D$; this peak indicates the enhanced probability of finding touching particle pairs in the turbulent flow compared with randomly distributed particles. As the separation distance r increases, the RDF quickly decreases to $g(r) = 1$, indicating a rapid decorrelation of particle locations. As regards the RRV, $\langle |W_r| \rangle$ is directly related to the particle velocity fluctuations for the largest separation distances (Jiang *et al.* 2026), so the value of $\langle |W_r| \rangle$ at $r \gtrsim 3D$ decreases with the Galileo number (shown in figure 15*b*) owing to the reduced particle velocity fluctuations (see figure 5*a*). At small separations, instead, the particle relative motion is dominated by the interparticle hydrodynamic interactions. The RRV decreases rapidly as the separation distance approaches $r \approx D$ owing to the significant lubrication effects among nearby particles (Jiang *et al.* 2024*b*). In addition, it is noteworthy that the value of $\langle |W_r(r = D)| \rangle$ is highest at $Ga = 120$ among all cases, which explains the highest collision kernel shown in figure 14 for the highest-Ga case, although the value of $g(r = D)$ is slightly reduced at $Ga = 120$ (see the inset in figure 15*a*).

At last, to further examine the effect of gravity on the particle-pair dynamics, we compute the particle-pair correlation function $g(r, \psi)$ and the absolute RRV $|W_r(r, \psi)|$ as two-dimensional functions of the independent variables r (the radial separation) and ψ (the polar angle relative to the vertical direction). This allows us to further understand the directional information about the particle spatial distribution and relative motions.

https://doi.org/10.1017/jfm.2026.11476 Published online by Cambridge University Press

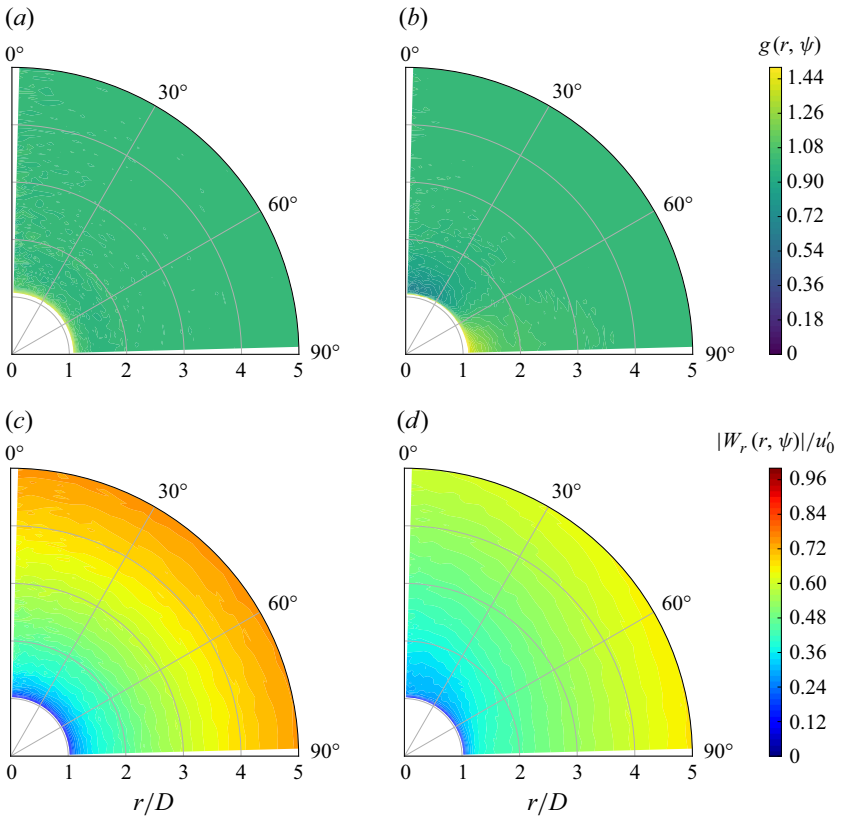


Figure 16. (*a*,*b*) The particle pair distribution function and (*c*,*d*) relative particle velocity at (*a*,*c*) $Ga = 0$ and (*b*,*d*) $Ga = 120$ as function of the distance r and the angle ψ.

Note that one can obtain the one-dimensional functions $g(r)$ and $\langle|W_r(r)|\rangle$ by integrating $g(r, \psi)$ and $|W_r(r, \psi)|$ over the polar angle ψ as (Yin & Koch 2007)

$$g(r) = \frac{1}{2}\int_0^\pi g(r, \psi)\sin\psi \mathrm{d}\psi, \tag{3.20}$$

$$\langle|W_r(r)|\rangle = \frac{1}{2}\int_0^\pi |W_r(r, \psi)| g(r, \psi)\sin\psi \mathrm{d}\psi. \tag{3.21}$$

The functions $g(r, \psi)$ and $|W_r(r, \psi)|$ are depicted in figure 16 for the suspensions at $Ga = 0$ (no gravity) and $Ga = 120$ (strongest particle sedimentation). As shown in figure 16(*a*,*c*), $g(r, \psi)$ and $|W_r(r, \psi)|$ only vary with the radial separation r for non-sedimenting particles ($Ga = 0$), and do not exhibit any directional preference. In contrast, at $Ga = 120$, we can clearly observe a directional bias in the spatial distribution and relative motion of particle pairs due to the sedimentation. Specifically, the data in figure 16(*b*) show that the probability of finding particle pairs along the horizontal direction is higher than that in the vertical direction, which could be related to the wake-induced hydrodynamic interactions among settling particles. This observation reminds us of the horizontally aligned particles settling in a quiescent fluid at a low Galileo number $Ga \approx 18$ (Yin & Koch 2007), but is in contrast to the column-like particle structures observed in settling-particle suspensions at high Ga (Uhlmann & Doychev 2014). The different behaviours may

https://doi.org/10.1017/jfm.2026.11476 Published online by Cambridge University Press

be ascribed to the complexity of the DKT-like interactions at different particle Reynolds numbers or in the turbulent/non-turbulent environments.

Regarding the particle relative motion (cf. figure 16*d*), the value of $|W_r(r, \psi)|$ is found to be greater for the horizontally aligned particle pairs ($\psi = 90°$) than for the vertically aligned ones ($\psi = 90°$) with a given radial separation distance r. Note that the directional preference of $|W_r(r, \psi)|$ observed in the current study is opposite to that observed for settling particles in a quiescent fluid: $|W_r(r, \psi)|$ was found to be greater along the vertical direction than horizontal direction for settling particles in the absence of background turbulence (see e.g. figure 8*e* in Jiang *et al.* 2026). This difference is reminiscent of the opposite variation of the particle vertical velocity fluctuations as Ga increases in turbulent and quiescent fluids (see the discussion in § 3.2). The decrease of $\sigma(v_y)$ at $Ga = 120$ (see figure 5*a*) is related to the smaller particle relative velocities along the vertical direction shown in figure 16(*d*), since the particle vertical velocity fluctuations can promote relative motion between the vertical-aligned particles. Moreover, considering the relationship (3.21), the large values of $g(r, \psi)$ and $|W_r(r, \psi)|$ in the region $(r, \psi) \approx (D, 90°)$ explain the higher value of $\langle |W_r(r = D)| \rangle$ in the suspension with $Ga = 120$ than for the non-sedimenting particles; this also results in an enhanced collision rate in the presence of gravitational sedimentation.

4. Concluding remarks

In this work, we have studied the gravity-driven sedimentation of spherical particles in sustained homogeneous and isotropic turbulence and the related turbulent modulation using PR-DNS. The particle size is an order of magnitude larger than the Kolmogorov length scale of the single-phase turbulent flow and the suspension volume fraction is fixed at 10 %. The effect of the particle sedimentation is studied by varying the value of the Galileo number of settling particles, which is achieved by changing the particle–fluid density ratios.

By computing the statistics of the turbulent flow, we find a reduced turbulence Taylor Reynolds number with the increase of the particle sedimentation speed because of the enhanced viscous dissipation induced by settling particles. The vorticity structures become fragmented, as confirmed by reduced Kolmogorov length scales, as the Galileo number increases. The interactions between settling particles and the turbulent flow result in higher fluid velocity fluctuations along the vertical direction than the horizontal one. Interestingly, the opposite is true for the velocity fluctuations of the solid phase: the reduced particle vertical velocity fluctuations are explained by the filtering of the background turbulent structures by the particle settling motions. Moreover, the average settling velocity of the particle phase is found to decrease when compared with that of the isolated settling particle in a quiescent fluid. The combined effects of hindrance in suspension and of the turbulence-induced drag increase are the reasons for the sedimentation attenuation. The latter effect becomes weaker as the ratio of the particle settling velocity to the turbulence velocity fluctuation velocity increases, i.e. increasing Ga.

To further explore the energy transfer of the turbulence modulated by particles, we have also investigated the energy spectra and SBS energy budget of the turbulent flows in the spectral space. Compared with the single-phase turbulence, the particles extract energy from large scales and reinject it at small scales, i.e. we observe a complementary energy cascade caused by the particle–fluid interactions, as in the bubble/droplet laden flows without gravity. This is shown by the presence of the κ^{-3} scaling of the energy spectra close to the particle scale. With the introduction of gravitational sedimentation, the settling motion of the particle phase plays an additional role in injecting energy into the fluid flow.

https://doi.org/10.1017/jfm.2026.11476 Published online by Cambridge University Press

The energy input by the particle sedimentation is proportional to the square of the Galileo number, and becomes the major energy source for the case with the highest Galileo number $Ga = 120$, approximately four times the energy injected by the large-scale external forces. In addition, as the Galileo number increases, the κ^{-3} scaling of the energy spectra is seen over a wider range of scales, cancelling the classic energy cascade (characterized by the $\kappa^{-5/3}$ scaling) in the inertial range at $Ga = 120$. The κ^{-3} scaling of the energy spectra is found to be associated with an almost direct balance between the energy injection by the fluid–solid interactions and viscous dissipation.

To better understand the directional information of the turbulence modulation, the spectral analyses of the energy and its SBS budget analysis are also performed in cylinder coordinates in spectral space. With the introduction of the particle sedimentation, the interactions between settling particles and the carrier flows break the isotropy of the energy distribution, which is seen in the single-phase turbulence or the non-sedimenting particle-laden turbulence. This kind of anisotropy is characterized by the slow decay of the energy spectral density along the horizontal wavenumber on large scales, and is related to the flow structures induced by settling particles. In particular, the settling particles create elongated vertically aligned wakes while disrupting the horizontal correlations of the flow structures when falling through them. Nevertheless, the flow recovers isotropy at small scales. In the cases where the particle sedimentation is non-negligible, the energy input by the particle sedimentation is maximized near the particle scale. For a sufficiently high particle settling speed, the energy injected by this mechanism is also found to be transferred outwards by the nonlinear effect at intermediate scales.

At last, we have also investigated the spatial distribution and collision rate of the dispersed particles. By means of the Voronoi tessellation analysis, we identity a moderate particle clustering in the turbulent flow, a phenomenon hardly affected by the particle sedimentation. As regards the particle collision rate, the collision kernel is found to vary non-monotonically, yet not considerably in absolute value, with increasing Galileo number. Further examination of the particle pair statistics, i.e. the RDF and the RRV (only functions of the particle relative distance), reveals that the increased particle collision rate at high Ga is mainly caused by the enhanced particle–particle relative motions. By scrutinizing the particle pair statistics as function of distance and angle with respect to the gravity direction, we find that, when sedimentation is significant, nearby particle pairs tend to align horizontally under the interparticle hydrodynamic interactions. These horizontally arranged particle pairs tend to have greater relative motions than those aligned vertically, which explains the enhanced RRV of nearby particle pairs at a high Galileo number. This also demonstrates the importance of a complete anisotropic analysis to unveil the features of particle dynamics.

To conclude, in this paper, we have demonstrated the essential role of the gravitational sedimentation in the modulation of the particle-laden turbulent flows. However, we have only studied the effect of particle sedimentation by changing the particle density. The other relevant effects, like the particle size, particle inertia, volume fraction and particle shape (Voth & Soldati 2017; Peng *et al.* 2023), are not addressed in the current work. In particular, whether the small-scale Kolmogorov scaling of the energy spectra (as shown in the bubble-induced turbulence by Ma *et al.* (2025)) will appear in particle-laden turbulence at high Galileo numbers, as well as its potential interaction with the background turbulence, needs to be explored. Additionally, how the turbulence modulation is altered by the clustering of settling particles at high Ga but low ϕ (see e.g. Chouippe & Uhlmann 2019) remains unknown. Finally, it is of interest to examine the potential usefulness of the non-dimensional parameter Λ (see (3.15)) to predict turbulence modulation in such scenarios. Moreover, the change of the local flow topology by the presence of settling

https://doi.org/10.1017/jfm.2026.11476 Published online by Cambridge University Press

particles (see recent studies by Chiarini & Rosti (2024) and Chiarini *et al.* (2025)) is worthy of further examination in future studies.

Funding. This research was funded by the Department of Energy and Process Engineering, Norwegian University of Science and Technology (NTNU), Norway and by Politecnico di Torino, Italy.

Declaration of interests. The authors report no conflict of interest.

Appendix A. Particle budget

In this appendix, we provide the detailed derivation of (3.13). As introduced in the main text, the contribution from the fluid–particle interactions to the total fluid-energy budget is caused by the work of the IBM forces, i.e.

$$\Psi_p = \left\langle \boldsymbol{f}_{ib} \cdot \boldsymbol{u} \right\rangle_{\Omega} . \tag{A1}$$

To establish the link between Ψ_p and the particle dynamics, we reformulate the equation above as follows (Chouippe & Uhlmann 2015):

$$\begin{aligned} \Psi_p &= \left\langle \boldsymbol{f}_{IB} \cdot \boldsymbol{u} \right\rangle_{\Omega} \\ &= \frac{1}{V_{\Omega}} \int_{\Omega} \boldsymbol{f}_{IB} \cdot \boldsymbol{u} \mathrm{d}\Omega \\ &\approx \frac{1}{V_{\Omega}} \sum_{i=1}^{N_p} \int_{\partial \Omega_p^i} \boldsymbol{F}_{IB}^i \cdot \boldsymbol{U}^i \mathrm{d}S. \end{aligned} \tag{A2}$$

Here, the capitalized variables represent Lagrangian quantities defined on the Lagrangian points on the particle surface, and the superscript i ($i = 1, 2, \cdot s, N_p$) denotes the specific particle. The conservation of momentum between the Eulerian and the Lagrangian representations of the IBM forces is applied for the derivation above (Peskin 2002; Breugem 2012), and the surface velocity $\boldsymbol{U}^i$ is computed by the rigid-motion of the particle,

$$\boldsymbol{U}^i = \boldsymbol{v}_p^i + \boldsymbol{\omega}^i \times \boldsymbol{r}, \tag{A3}$$

where $\boldsymbol{r} = \boldsymbol{X} - \boldsymbol{x}_c^i$ is the vector from the particle centroid to a point on the particle surface. By inserting (A3) into (A2) and using the relationship $\phi = N_p V_p / V_{\Omega}$ and $(\boldsymbol{\omega}_p \times \boldsymbol{r}) \cdot \boldsymbol{F_{IB}} = \boldsymbol{\omega}_p \cdot (\boldsymbol{r} \times \boldsymbol{F_{IB}})$, we arrive at

$$\begin{aligned} \Psi_p &\approx \frac{1}{V_{\Omega}} \sum_{i=1}^{N_p} \int_{\partial \Omega_p^i} \boldsymbol{F}_{IB}^i \cdot \boldsymbol{U}^i \mathrm{d}S \\ &= \frac{\phi}{V_p} \frac{1}{N_p} \sum_{i=1}^{N_p} \left[\boldsymbol{v}^i \cdot \int_{\partial \Omega_p^i} \boldsymbol{F}_{IB}^i \mathrm{d}S + \boldsymbol{\omega}^i \cdot \int_{\partial \Omega_p^i} \boldsymbol{r} \times \boldsymbol{F}_{IB}^i \mathrm{d}S \right] \\ &= \frac{\phi}{V_p} \left\langle \boldsymbol{v} \cdot \int_{\partial \Omega_p} \boldsymbol{F}_{IB} \mathrm{d}S + \boldsymbol{\omega} \cdot \int_{\partial \Omega_p} \boldsymbol{r} \times \boldsymbol{F}_{IB} \mathrm{d}S \right\rangle_p . \end{aligned} \tag{A4}$$

https://doi.org/10.1017/jfm.2026.11476 Published online by Cambridge University Press

To proceed, let us reintroduce the Newton–Euler equations ((2.3)–(2.4)),

$$\rho_p V_p \frac{\mathrm{d}\boldsymbol{v}}{\mathrm{d}t} = -\int_{\partial\Omega_p} \rho_f \boldsymbol{F}_{IB}\mathrm{d}S + \rho_f \frac{d}{\mathrm{d}t}\int_{\Omega_f} \boldsymbol{u}\mathrm{d}V - \int_{\Omega_p} \rho_f \boldsymbol{f}_{ext}\mathrm{d}V + \left(\rho_p - \rho_f\right)\boldsymbol{g}V_p + \boldsymbol{F}_C \tag{A5}$$

$$I_p \frac{\mathrm{d}\boldsymbol{\omega}}{\mathrm{d}t} = -\rho_f \oint_{\partial\Omega_p^i} \boldsymbol{r}\times\boldsymbol{F}_{IB}\mathrm{d}S + \rho_f \frac{d}{\mathrm{d}t}\int_{\Omega_p} \boldsymbol{r}\times\boldsymbol{u}\mathrm{d}V + \boldsymbol{T}_C. \tag{A6}$$

In the above equations, the hydrodynamic force ($\boldsymbol{F}_H$) and torque ($\boldsymbol{T}_H$) are replaced by the integral of the IBM forces obtained by integrating the momentum (2.2) over the volume occupied by the particle (Breugem 2012),

$$\begin{aligned}\boldsymbol{F}^H &= \int_{\partial\Omega_p} \boldsymbol{\tau}\cdot\boldsymbol{n}\mathrm{d}S \\ &= -\rho_f\int_{\partial\Omega_p}\boldsymbol{F}_{IB}\mathrm{d}S + \rho_f\frac{d}{\mathrm{d}t}\int_{\Omega_{p(t)}}\boldsymbol{u}\mathrm{d}V - \rho_f\int_{\Omega_p}\boldsymbol{f}_{ext}\mathrm{d}V,\end{aligned} \tag{A7}$$

$$\begin{aligned}\boldsymbol{T}_H &= \int_{\partial\Omega_p} \boldsymbol{r}\times\boldsymbol{\tau}\cdot\boldsymbol{n}\mathrm{d}S \\ &= -\rho_f\int_{\partial\Omega_p}\boldsymbol{r}\times\boldsymbol{F}_{IB}\mathrm{d}S + \rho_f\frac{d}{\mathrm{d}t}\int_{\Omega_p}\boldsymbol{r}\times\boldsymbol{u}\mathrm{d}V - \rho_f\int_{\Omega_p}\boldsymbol{r}\times\boldsymbol{f}_{ext}\mathrm{d}V.\end{aligned} \tag{A8}$$

Note that the external forces needed to sustain the turbulence (i.e. the last term in the above two equations) also contributes to the hydrodynamic force and torque on the particle, since the forcing term $\boldsymbol{f}_{ext}$ is also applied in the space occupied by the dispersed particles.

By multiplying (A5) with the particle velocity $\boldsymbol{v}$ and computing the average over all particles, we can write

$$\begin{aligned}\rho_p V_p \frac{d}{\mathrm{d}t}\left\langle\frac{1}{2}\boldsymbol{v}\cdot\boldsymbol{v}\right\rangle_p = &-\rho_f\left\langle\boldsymbol{v}\cdot\int_{\partial\Omega_p}\boldsymbol{F}_{IB}\mathrm{d}S\right\rangle_p + \rho_f\left\langle\boldsymbol{v}\cdot\frac{d}{\mathrm{d}t}\int_{\Omega_p}\boldsymbol{u}\mathrm{d}V\right\rangle_p \\ &-\rho_f\left\langle\boldsymbol{v}\cdot\int_{\Omega_p}\boldsymbol{f}_{ext}\mathrm{d}V\right\rangle_p + \left(\rho_p-\rho_f\right)\langle\boldsymbol{v}\rangle_p\cdot\boldsymbol{g}V_p + \langle\boldsymbol{v}\cdot\boldsymbol{F}_C\rangle_p .\end{aligned} \tag{A9}$$

The above equation describes the contributions to the temporal evolution of the mean translational kinetic energy of the particle phase. If we now introduce the assumption of rigid-body motion for the flow inside the particle, the second term on the right-hand side of (A9) can be reformulated as (Uhlmann 2005)

$$\rho_f\left\langle\boldsymbol{v}\cdot\frac{d}{\mathrm{d}t}\int_{\Omega_p}\boldsymbol{u}\mathrm{d}V\right\rangle_p \approx \rho_f\left\langle\boldsymbol{v}\cdot\frac{\mathrm{d}\boldsymbol{v}}{\mathrm{d}t}V_p\right\rangle_p = \rho_f V_p\frac{d}{\mathrm{d}t}\left\langle\frac{1}{2}\boldsymbol{v}\cdot\boldsymbol{v}\right\rangle_p . \tag{A10}$$

By inserting (A10) into (A9), we obtain after some algebraic manipulations,

$$\begin{aligned}\left\langle\boldsymbol{v}\cdot\int_{\partial\Omega_p}\boldsymbol{F}_{IB}\mathrm{d}S\right\rangle_p \approx &\left(\frac{\rho_p}{\rho_f}-1\right)V_p\left[\langle\boldsymbol{v}\rangle_p\cdot\boldsymbol{g} - \frac{d}{\mathrm{d}t}\left\langle\frac{1}{2}\boldsymbol{v}\cdot\boldsymbol{v}\right\rangle_p\right] \\ &-\left\langle\boldsymbol{v}\cdot\int_{\Omega_p}\boldsymbol{f}_{ext}\mathrm{d}V\right\rangle_p + \frac{1}{\rho_f}\langle\boldsymbol{v}\cdot\boldsymbol{F}_C\rangle_p .\end{aligned} \tag{A11}$$

https://doi.org/10.1017/jfm.2026.11476 Published online by Cambridge University Press

Similar steps can be performed for the rotational dynamics of the particles, yielding

$$\left\langle \boldsymbol{\omega} \cdot \int_{\partial \Omega_p} \boldsymbol{r} \times \boldsymbol{F}_{IB} \mathrm{d}S \right\rangle_p = \frac{1}{\rho_p} \left(1 - \frac{\rho_p}{\rho_f}\right) I_p \frac{d}{\mathrm{d}t} \left\langle \frac{1}{2} \boldsymbol{\omega}_p \cdot \boldsymbol{\omega}_p \right\rangle_p - \left\langle \boldsymbol{\omega} \cdot \int_{\Omega_p} \boldsymbol{r} \times \boldsymbol{f}_{ext} \mathrm{d}V \right\rangle_p + \frac{1}{\rho_f} \langle \boldsymbol{\omega} \cdot \boldsymbol{T}_C \rangle_p. \tag{A12}$$

Inserting (A11) and (A12) into (A4), we can finally arrive at

$$\begin{aligned} \Psi_p \approx & -\frac{\phi}{\rho_p V_p} \left(\frac{\rho_p}{\rho_f} - 1\right) \left[\rho_p V_p \frac{d}{\mathrm{d}t} \left\langle \frac{1}{2} \boldsymbol{v} \cdot \boldsymbol{v} \right\rangle_p + I_p \frac{d}{\mathrm{d}t} \left\langle \frac{1}{2} \boldsymbol{\omega}_p \cdot \boldsymbol{\omega}_p \right\rangle_p \right] \\ & + \phi \left(\frac{\rho_p}{\rho_f} - 1\right) \langle \boldsymbol{v} \rangle_p \cdot \boldsymbol{g} + \frac{\phi}{\rho_f V_p} \left[\langle \boldsymbol{v} \cdot \boldsymbol{F}_C \rangle_p + \langle \boldsymbol{\omega} \cdot \boldsymbol{T}_C \rangle_p \right] \\ & - \frac{\phi}{V_p} \left\langle \boldsymbol{v} \cdot \int_{\Omega_p} \boldsymbol{f}_{ext} \mathrm{d}V + \boldsymbol{\omega} \cdot \int_{\Omega_p} \boldsymbol{r} \times \boldsymbol{f}_{ext} \mathrm{d}V \right\rangle_p, \end{aligned} \tag{A13}$$

which is identical to (3.13) in the main text.

Appendix B. Discussion on the particle-induced dissipation

In this appendix, we further look into the particle-induced dissipation and examine the contribution from Ψ_p^{ext} to the particle budget (see (3.13)). To this end, we conducted an additional simulation for the case with $Ga = 0$ (no sedimentation). The difference of this additional simulation (which is referred to as case 1A for brevity hereinafter) from case 1 reported in the main text is that we set the external forces used to sustain the background turbulence to zero in the volume occupied by the dispersed particles. In other words, the forcing term $\boldsymbol{f}_{ext}$ in (2.2) is applied only in the region occupied by the fluid phase. To keep the energy input unchanged, we compensate the energy loss due to the spatial filtering of the external forces by amplifying the magnitude of the forcing by the factor $1/(1-\phi)$ (Peng *et al.* 2023), i.e. $\epsilon^*_{exc} = (1/1-\phi)\epsilon^*_{inc}$, where ϵ^* denotes the magnitude of the EP forces (see table 1) and the subscripts 'exc' and 'inc' denote the exclusion or inclusion of the volume occupied by the solid phase. Note that, to run this additional case, we restart the simulation from the checkout data of the original case 1 at $t = 32.94T_e$.

Figure 17 illustrates the time history of the Taylor Reynolds number in the simulation of cases 1 and 1A. We can observe an almost unchanged mean value of Re_λ before and after the restart of the simulation, suggesting a negligible effect of the specific way the external force is applied on the single-point statistics of the modulated turbulence.

Most importantly, we compare the SBS budget of the turbulent flow under these two conditions, with the results shown in figure 18. The most relevant difference is the reduction of the contribution from the particle–fluid interactions, i.e. the term $\mathcal{F}_{ib}^{\Sigma}$, when the external forces are limited to the fluid phase (the red dashed line in figure 18). In particular, the value of $\mathcal{F}_{ib}^{\Sigma}(\kappa = \kappa_{max})$ is almost zero in case 1A, indicating the zero net contribution from the particle–fluid interactions to the fluid energy budget. This observation is consistent with the result reported in Chiarini & Rosti (2024) among others.

To elucidate the difference between case 1 and 1A, we revisit the particle budget given by (3.13). Since the external force is excluded from the space occupied by the dispersed particles in case 1A, the integrals defining the term Ψ_p^{ext} become zero, leading to the vanishing value of Ψ_p^{ext}. This is in contrast to the negative value of Ψ_p^{ext} due to the

https://doi.org/10.1017/jfm.2026.11476 Published online by Cambridge University Press

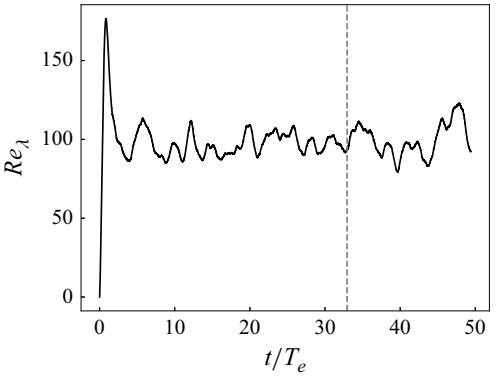


Figure 17. Time history of the Taylor Reynolds number Re_λ for the case with $Ga = 0$. The original simulation (with external forces applied inside the solid phase) ends at $t = 32.94T_e$ (displayed by the vertical dashed line). After this instant, the simulation is restarted with external forces of increased magnitude only in the volume occupied by the fluid phase. Time is normalized by $T_e = u'^2/\epsilon$, the integral time scale pertaining to this case.

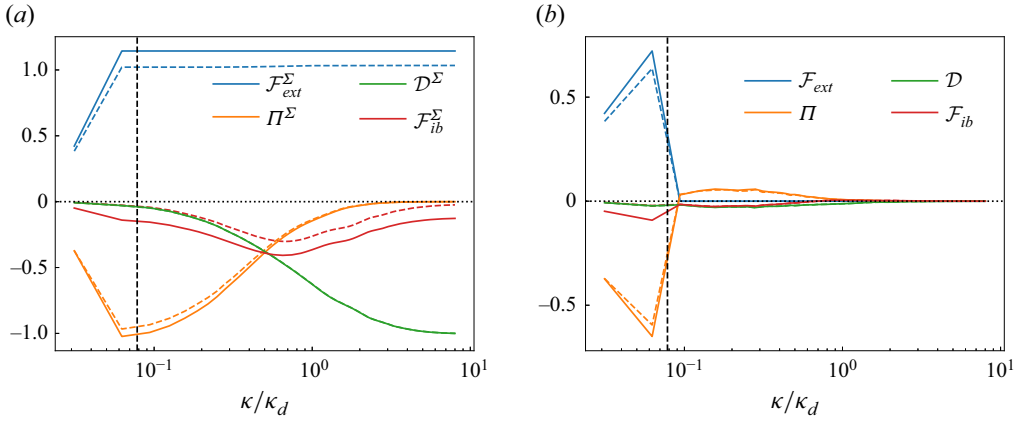


Figure 18. (*a*) Cumulative and (*b*) non-cumulative SBS energy budget for the suspension of spherical particles with $Ga = 0$. The solid lines represent the results with the external forces needed to sustain the turbulence also applied inside the solid phase (the same as in figure 7*a*), while the dashed lines are the results limiting these forces to the fluid phase. The total viscous dissipation $\mathcal{D}^\Sigma_{tot} = -\sum_{\kappa=0}^{\kappa_{max}} \mathcal{D}(\kappa)$ is used to normalize the data.

positive correlation between the particle motion and large-scale external forces in case 1 as discussed in the main text. Note additionally that the small residual value of $\mathcal{F}_{ib}(\kappa = \kappa_{max})$ in case 1A (see the last point of the red dashed line in figure 18*a*) is related to the contribution from the particle–particle collisions (the term Ψ_p^{col} in (3.13)).

By scrutinizing the red solid and dashed lines in figure 18(*a*), we can find that the difference of the spectra of the IB forcing term are mainly originated from large scales. In case 1 (indicated by the red solid line), $\mathcal{F}^\Sigma_{ib}$ grows more rapidly in amplitude before the cutoff wavenumber ($\kappa < \kappa_f$). Above the cutoff wavenumber, the variation of the cumulative spectrum $\mathcal{F}^\Sigma_{ib}$ is almost the same for the two cases, suggesting that the particle–fluid interactions are not affected by the different external forces at smaller scales (the solid and dashed lines almost maintain the same distance). This is more evident when examining the non-cumulative budget terms, see (2.6) in the main text, as depicted in figure 18(*b*). Moreover, note that to close the energy budget, the contribution of the external force (the

https://doi.org/10.1017/jfm.2026.11476 Published online by Cambridge University Press

term $\mathcal{F}_{ext}^{\Sigma}$) also decreases in case 1A (the dashed blue line) when compared with case 1 (the solid blue line).

To conclude, the aforementioned result demonstrates that the influence of the forcing strategy on the single-point statistics of the turbulence is negligible. As concerns the energy budget, although the inclusion of the external forcing term inside the particle phase results in a net particle-induced dissipation, this contribution is subdominant compared with the fluid viscous dissipation, and has a negligible effect on the energy budget on scales smaller than those of the external forces.

Moreover, if we further consider the particle sedimentation, the contribution from Ψ_p^{ext} would be overcome by the positive work done by the gravity settling (i.e. the term Ψ_p^{gra} in (3.13)) in configurations with fast particle settling speed. In conclusion, we believe that simulations performed with the external forcing term also in the solid phase provide physically meaningful results and shed light on the energy transfer mechanisms in particle-laden turbulent flows.

References

Aliseda, A., Cartellier, A., Hainaux, F. & Lasheras, J.C. 2002 Effect of preferential concentration on the settling velocity of heavy particles in homogeneous isotropic turbulence. *J. Fluid Mech.* **468**, 77–105.

Amoura, Z., Besnaci, C., Risso, F. & Roig, V. 2017 Velocity fluctuations generated by the flow through a random array of spheres: a model of bubble-induced agitation. *J. Fluid Mech.* **823**, 592–616.

Ardekani, M.N., Sardina, G., Brandt, L., Karp-Boss, L., Bearon, R. & Variano, E. 2017 Sedimentation of inertia-less prolate spheroids in homogenous isotropic turbulence with application to non-motile phytoplankton. *J. Fluid Mech.* **831**, 655–674.

Balachandar, S. & Eaton, J.K. 2010 Turbulent dispersed multiphase flow. *Annu. Rev. Fluid Mech.* **42**, 111–133.

Balachandar, S., Peng, C. & Wang, L.-P. 2024 Turbulence modulation by suspended finite-sized particles: toward physics-based multiphase subgrid modeling. *Phys. Rev. Fluids* **9** (4), 044304.

Bhattacharjee, S., Tom, J., Carbone, M. & Bragg, A.D. 2024 Investigating the parametric dependence of the impact of two-way coupling on inertial particle settling in turbulence. *J. Fluid Mech.* **987**, A17.

Boivin, M., Simonin, O. & Squires, K.D. 1998 Direct numerical simulation of turbulence modulation by particles in isotropic turbulence. *J. Fluid Mech.* **375**, 235–263.

Bosse, T., Kleiser, L. & Meiburg, E. 2006 Small particles in homogeneous turbulence: settling velocity enhancement by two-way coupling. *Phys. Fluids* **18** (2), 027102.

Botto, L. & Prosperetti, A. 2012 A fully resolved numerical simulation of turbulent flow past one or several spherical particles. *Phys. Fluids* **24** (1), 013303.

Brandt, L. & Coletti, F. 2022 Particle-laden turbulence: progress and perspectives. *Annu. Rev. Fluid Mech.* **54** (1), 159–189.

Breugem, W.-P. 2012 A second-order accurate immersed boundary method for fully resolved simulations of particle-laden flows. *J. Comput. Phys.* **231** (13), 4469–4498.

Chiarini, A. & Rosti, M.E. 2024 Finite-size inertial spherical particles in turbulence. *J. Fluid Mech.* **988**, A17.

Chiarini, A., Tandurella, S. & Rosti, M.E. 2025 Kolmogorov-size particles in homogeneous and isotropic turbulence. *J. Fluid Mech.* **1007**, A81.

Chouippe, A. & Uhlmann, M. 2015 Forcing homogeneous turbulence in direct numerical simulation of particulate flow with interface resolution and gravity. *Phys. Fluids* **27** (12), 123301.

Chouippe, A. & Uhlmann, M. 2019 On the influence of forced homogeneous-isotropic turbulence on the settling and clustering of finite-size particles. *Acta Mechanica* **230**, 387–412.

Cisse, M., Homann, H. & Bec, J. 2013 Slipping motion of large neutrally buoyant particles in turbulence. *J. Fluid Mech.* **735**, R1.

Costa, P., Boersma, B.J., Westerweel, J. & Breugem, W.-P. 2015 Collision model for fully resolved simulations of flows laden with finite-size particles. *Phys. Rev. E* **92** (5), 053012.

Crialesi-Esposito, M., Rosti, M.E., Chibbaro, S. & Brandt, L. 2022 Modulation of homogeneous and isotropic turbulence in emulsions. *J. Fluid Mech.* **940**, A19.

Davis, R.H. & Acrivos, A. 1985 Sedimentation of noncolloidal particles at low Reynolds numbers. *Annu. Rev. Fluid Mech.* **17**, 97–118.

https://doi.org/10.1017/jfm.2026.11476 Published online by Cambridge University Press

DODD, M.S. & FERRANTE, A. 2016 On the interaction of Taylor length scale size droplets and isotropic turbulence. *J. Fluid Mech.* **806**, 356–412.
ELGHOBASHI, S. & TRUESDELL, G. 1993 On the two-way interaction between homogeneous turbulence and dispersed solid particles. I: turbulence modification. *Phys. Fluids* **5** (7), 1790–1801.
ESWARAN, V. & POPE, S. 1988 An examination of forcing in direct numerical simulations of turbulence. *Comput. Fluids* **16** (3), 257–278.
FERRANTE, A. & ELGHOBASHI, S. 2003 On the physical mechanisms of two-way coupling in particle-laden isotropic turbulence. *Phys. Fluids* **15** (2), 315–329.
FIABANE, L., ZIMMERMANN, R., VOLK, R., PINTON, J.-F. & BOURGOIN, M. 2012 Clustering of finite-size particles in turbulence. *Phys. Rev. E* **86** (3), 035301.
FORNARI, W., ARDEKANI, M.N. & BRANDT, L. 2018 Clustering and increased settling speed of oblate particles at finite Reynolds number. *J. Fluid Mech.* **848**, 696–721.
FORNARI, W., PICANO, F. & BRANDT, L. 2016*a* Sedimentation of finite-size spheres in quiescent and turbulent environments. *J. Fluid Mech.* **788**, 640–669.
FORNARI, W., PICANO, F., SARDINA, G. & BRANDT, L. 2016*b* Reduced particle settling speed in turbulence. *J. Fluid Mech.* **808**, 153–167.
FORNARI, W., ZADE, S., BRANDT, L. & PICANO, F. 2019 Settling of finite-size particles in turbulence at different volume fractions. *Acta Mechanica* **230** (2), 413–430.
FRISCH, U. 1995 *Turbulence: The Legacy of A. N. Kolmogorov*. Cambridge University Press.
GARSIDE, J. & AL-DIBOUNI, M.R. 1977 Velocity-voidage relationships for fluidization and sedimentation in solid–liquid systems. *Ind. Engng Chem. Process Des. Develop.* **16** (2), 206–214.
GORE, R. & CROWE, C. 1989 Effect of particle size on modulating turbulent intensity. *Intl J. Multiphase Flow* **15** (2), 279–285.
GOTO, S. & VASSILICOS, J.C. 2008 Sweep-stick mechanism of heavy particle clustering in fluid turbulence. *Phys. Rev. Lett.* **100** (5), 054503.
GUAZZELLI, E. & MORRIS, J.F. 2011 *A Physical Introduction to Suspension Dynamics*, vol. 45. Cambridge University Press.
HESSENKEMPER, H., BRAGG, A.D., LUCAS, D. & MA, T. 2025 Lagrangian tracking reveals competing influences of clustering and turbulence on the rise velocity of bubble swarms. *Proc. Natl Acad. Sci. USA* **122** (48), e2518309122.
HETSRONI, G. 1989 Particles-turbulence interaction. *Intl J. Multiphase Flow* **15** (5), 735–746.
HÖFLER, K. & SCHWARZER, S. 2000 Navier–Stokes simulation with constraint forces: finite-difference method for particle-laden flows and complex geometries. *Phys. Rev. E* **61** (6), 7146–7160.
HOMANN, H. & BEC, J. 2010 Finite-size effects in the dynamics of neutrally buoyant particles in turbulent flow. *J. Fluid Mech.* **651**, 81–91.
HOMANN, H., BEC, J. & GRAUER, R. 2013 Effect of turbulent fluctuations on the drag and lift forces on a towed sphere and its boundary layer. *J. Fluid Mech.* **721**, 155–179.
HUCK, P.D., BATESON, C., VOLK, R., CARTELLIER, A., BOURGOIN, M. & ALISEDA, A. 2018 The role of collective effects on settling velocity enhancement for inertial particles in turbulence. *J. Fluid Mech.* **846**, 1059–1075.
HWANG, W. & EATON, J.K. 2006 Homogeneous and isotropic turbulence modulation by small heavy ($St \sim 50$) particles. *J. Fluid Mech.* **564**, 361.
INNOCENTI, A., JACCOD, A., POPINET, S. & CHIBBARO, S. 2021 Direct numerical simulation of bubble-induced turbulence. *J. Fluid Mech.* **918**, A23.
JEFFREY, D.J. 1982 Low-Reynolds-number flow between converging spheres. *Mathematika* **29** (1), 58–66.
JIANG, X., BRANDT, L., XU, C. & ZHAO, L. 2025 Pseudo-turbulence induced by settling spheroids in a quiescent fluid. *J. Fluid Mech.* **1011**, A22.
JIANG, X., HUANG, W., XU, C. & ZHAO, L. 2024*a* A flow-reconstruction based approach for the computation of hydrodynamic stresses on immersed body surface. *J. Comput. Phys.* **508**, 113025.
JIANG, X., XU, C. & ZHAO, L. 2024*b* Prolate spheroids settling in a quiescent fluid: clustering, microstructures and collisions. *J. Fluid Mech.* **1000**, A49.
JIANG, X., ZHAO, L. & BRANDT, L. 2026 On the dynamics of settling spheroidal particles. *Acta Mechanica Sin.* **42**, 725052.
JIN, G., WANG, Y., ZHANG, J. & HE, G. 2013 Turbulent clustering of point particles and finite-size particles in isotropic turbulent flows. *Ind. Engng Chem. Res.* **52** (33), 11294–11301.
KEMPE, T. & FRÖHLICH, J. 2012 An improved immersed boundary method with direct forcing for the simulation of particle laden flows. *J. Comput. Phys.* **231** (9), 3663–3684.
KIM, K., BAEK, S.-J. & SUNG, H.J. 2002 An implicit velocity decoupling procedure for the incompressible Navier–Stokes equations. *Intl J. Numer. Meth. Fluids* **38** (2), 125–138.

https://doi.org/10.1017/jfm.2026.11476 Published online by Cambridge University Press

LANCE, M. & BATAILLE, J. 1991 Turbulence in the liquid phase of a uniform bubbly air–water flow. *J. Fluid Mech.* **222**, 95–118.
LIU, H. 2024 Simple and accurate expressions for radial distribution functions of hard disk and hard sphere fluids. *Mol. Phys.* **122** (13), e2299250.
LUCCI, F., FERRANTE, A. & ELGHOBASHI, S. 2010 Modulation of isotropic turbulence by particles of Taylor length-scale size. *J. Fluid Mech.* **650**, 5–55.
LUCCI, F., FERRANTE, A. & ELGHOBASHI, S. 2011 Is Stokes number an appropriate indicator for turbulence modulation by particles of Taylor-length-scale size? *Phys. Fluids* **23** (2), 025101.
MA, T., TAN, S., NI, R., HESSENKEMPER, H. & BRAGG, A.D. 2025 Kolmogorov scaling in bubble-induced turbulence. *Phys. Rev. Lett.* **134** (24), 244001.
MARTÍNEZ MERCADO, J., CHEHATA GÓMEZ, D., VAN GILS, D., SUN, C. & LOHSE, D. 2010 On bubble clustering and energy spectra in pseudo-turbulence. *J. Fluid Mech.* **650**, 287–306.
MEHRABADI, M., TENNETI, S., GARG, R. & SUBRAMANIAM, S. 2015 Pseudo-turbulent gas-phase velocity fluctuations in homogeneous gas–solid flow: fixed particle assemblies and freely evolving suspensions. *J. Fluid Mech.* **770**, 210–246.
MONCHAUX, R., BOURGOIN, M. & CARTELLIER, A. 2010 Preferential concentration of heavy particles: a Voronoï analysis. *Phys. Fluids* **22** (10), 103304.
MONCHAUX, R., BOURGOIN, M. & CARTELLIER, A. 2012 Analyzing preferential concentration and clustering of inertial particles in turbulence. *Intl J. Multiphase Flow* **40**, 1–18.
MONCHAUX, R. & DEJOAN, A. 2017 Settling velocity and preferential concentration of heavy particles under two-way coupling effects in homogeneous turbulence. *Phys. Rev. Fluids* **2** (10), 104302.
MORICHE, M., HETTMANN, D., GARCÍA-VILLALBA, M. & UHLMANN, M. 2023 On the clustering of low-aspect-ratio oblate spheroids settling in ambient fluid. *J. Fluid Mech.* **963**, A1.
NASO, A. & PROSPERETTI, A. 2010 The interaction between a solid particle and a turbulent flow. *New J. Phys.* **12** (3), 033040.
OKA, S. & GOTO, S. 2022 Attenuation of turbulence in a periodic cube by finite-size spherical solid particles. *J. Fluid Mech.* **949**, A45.
PANDEY, V., MITRA, D. & PERLEKAR, P. 2023 Kolmogorov turbulence coexists with pseudo-turbulence in buoyancy-driven bubbly flows. *Phys. Rev. Lett.* **131** (11), 114002.
PANDEY, V., RAMADUGU, R. & PERLEKAR, P. 2020 Liquid velocity fluctuations and energy spectra in three-dimensional buoyancy-driven bubbly flows. *J. Fluid Mech.* **884**, R6.
PENG, C., KARZHAUBAYEV, K., WANG, L.-P., CHEN, S. & NIU, Z. 2025 Settling of finite-size particles in homogeneous isotropic turbulence: the influence of particle inertia and a unified predictive model. *J. Fluid Mech.* **1016**, A63.
PENG, C., SUN, Q. & WANG, L.-P. 2023 Parameterization of turbulence modulation by finite-size solid particles in forced homogeneous isotropic turbulence. *J. Fluid Mech.* **963**, A6.
PESKIN, C.S. 2002 The immersed boundary method. *Acta Numerica* **11**, 479–517.
PETERSEN, A.J., BAKER, L. & COLETTI, F. 2019 Experimental study of inertial particles clustering and settling in homogeneous turbulence. *J. Fluid Mech.* **864**, 925–970.
POELMA, C. & OOMS, G. 2006 Particle-turbulence interaction in a homogeneous, isotropic turbulent suspension. *Appl. Mech. Rev.* **59** (2), 78–90.
POPE, S.B. 2000 *Turbulent Flows*. Cambridge University Press.
PUMIR, A. & WILKINSON, M. 2016 Collisional aggregation due to turbulence. *Annu. Rev. Condens. Matt. Phys.* **7** (1), 141–170.
RICHARDSON, J. & ZAKI, W. 1954 The sedimentation of a suspension of uniform spheres under conditions of viscous flow. *Chem. Engng Sci.* **3** (2), 65–73.
SAFFMAN, P.G. & TURNER, J.S. 1956 On the collision of drops in turbulent clouds. *J. Fluid Mech.* **1**, 16–30.
SCHNEIDERS, L., MEINKE, M. & SCHRÖDER, W. 2017 Direct particle–fluid simulation of Kolmogorov-length-scale size particles in decaying isotropic turbulence. *J. Fluid Mech.* **819**, 188–227.
SHAW, R.A. 2003 Particle-turbulence interactions in atmospheric clouds. *Annu. Rev. Fluid Mech.* **35** (1), 183–227.
SHEN, J., PENG, C., WU, J., CHONG, K.L., LU, Z. & WANG, L.-P. 2022 Turbulence modulation by finite-size particles of different diameters and particle–fluid density ratios in homogeneous isotropic turbulence. *J. Turbul.* **23** (8), 433–453.
SMOLUCHOWSKI, M.V. 1917 Mathematical theory of the kinetics of the coagulation of colloidal solutions. *Z. Phys. Chem.-Intl J. Res. Phys. Chem. Chem. Phys.* **92**, 129–168.
SQUIRES, K.D. & EATON, J.K. 1990 Particle response and turbulence modification in isotropic turbulence. *Phys. Fluids* **2** (7), 1191–1203.

https://doi.org/10.1017/jfm.2026.11476 Published online by Cambridge University Press

SUNDARAM, S. & COLLINS, L.R. 1999 A numerical study of the modulation of isotropic turbulence by suspended particles. *J. Fluid Mech.* **379**, 105–143.

TAGAWA, Y., ROGHAIR, I., PRAKASH, V.N., VAN SINT ANNALAND, M., KUIPERS, H., SUN, C. & LOHSE, D. 2013 The clustering morphology of freely rising deformable bubbles. *J. Fluid Mech.* **721**, R2.

TANAKA, T. & EATON, J.K. 2010 Sub-Kolmogorov resolution partical image velocimetry measurements of particle-laden forced turbulence. *J. Fluid Mech.* **643**, 177–206.

TEN CATE, A., DERKSEN, J.J., PORTELA, L.M. & VAN DEN AKKER, H.E. 2004 Fully resolved simulations of colliding monodisperse spheres in forced isotropic turbulence. *J. Fluid Mech.* **519**, 233–271.

TOM, J., CARBONE, M. & BRAGG, A.D. 2022 How does two-way coupling modify particle settling and the role of multiscale preferential sweeping? *J. Fluid Mech.* **947**, A7.

UHLMANN, M. 2005 An immersed boundary method with direct forcing for the simulation of particulate flows. *J. Comput. Phys.* **209** (2), 448–476.

UHLMANN, M. 2020 Voronoï tessellation analysis of sets of randomly placed finite-size spheres. *Phys. A* **555**, 124618.

UHLMANN, M. & CHOUIPPE, A. 2017 Clustering and preferential concentration of finite-size particles in forced homogeneous-isotropic turbulence. *J. Fluid Mech.* **812**, 991–1023.

UHLMANN, M. & DOYCHEV, T. 2014 Sedimentation of a dilute suspension of rigid spheres at intermediate Galileo numbers: the effect of clustering upon the particle motion. *J. Fluid Mech.* **752**, 310–348.

VOTH, G.A. & SOLDATI, A. 2017 Anisotropic particles in turbulence. *Annu. Rev. Fluid Mech.* **49** (1), 249–276.

WANG, L.-P. 2023 Coagulation in turbulent particle-laden flows. In *Modeling Approaches and Computational Methods for Particle-Laden Turbulent Flows* (ed. S. SUBRAMANIAM & S. BALACHANDAR), Computation and Analysis of Turbulent Flows , pp.111–145. Academic Press.

WANG, L.-P., AYALA, O., GAO, H., ANDERSEN, C. & MATHEWS, K.L. 2014 Study of forced turbulence and its modulation by finite-size solid particles using the lattice boltzmann approach. *Comput. Math. Applics* **67** (2), 363–380.

WANG, L.-P. & MAXEY, M.R. 1993 Settling velocity and concentration distribution of heavy particles in homogeneous isotropic turbulence. *J. Fluid Mech.* **256**, 27–68.

WANG, L.-P., WEXLER, A.S. & ZHOU, Y. 2000 Statistical mechanical description and modelling of turbulent collision of inertial particles. *J. Fluid Mech.* **415**, 117–153.

XIA, Y., YU, Z., PAN, D., LIN, Z. & GUO, Y. 2022 Drag model from interface-resolved simulations of particle sedimentation in a periodic domain and vertical turbulent channel flows. *J. Fluid Mech.* **944**, A25.

YANG, T. & SHY, S. 2005 Two-way interaction between solid particles and homogeneous air turbulence: particle settling rate and turbulence modification measurements. *J. Fluid Mech.* **526**, 171–216.

YIN, X. & KOCH, D.L. 2007 Hindered settling velocity and microstructure in suspensions of solid spheres with moderate Reynolds numbers. *Phys. Fluids* **19** (9), 093302.

YU, Z., XIA, Y., GUO, Y. & LIN, Z. 2021 Modulation of turbulence intensity by heavy finite-size particles in upward channel flow. *J. Fluid Mech.* **913**, A3.

ZAIDI, A.A. 2018 Particle velocity distributions and velocity fluctuations of non-Brownian settling particles by particle-resolved direct numerical simulation. *Phys. Rev. E* **98** (5), 053103.

ZAIDI, A.A., TSUJI, T. & TANAKA, T. 2014 Direct numerical simulation of finite sized particles settling for high Reynolds number and dilute suspension. *Intl J. Heat Fluid Flow* **50**, 330–341.

https://doi.org/10.1017/jfm.2026.11476 Published online by Cambridge University Press